③

LEVEL II

SC

PSR Report 815

EFFECT OF BURIAL DEPTH ON SEISMIC SIGNALS

VOLUME I

May 1979

See 1473

N. Perl, Applied Theory, Inc.
F. J. Thomas, Pacific-Sierra Research Corp.
J. Trulio, Applied Theory, Inc.
W. L. Woodie, Pacific-Sierra Research Corp.

DDC
RECEIVED
JUN 13 1979
E

PACIFIC • SIERRA RESEARCH CORP.

1456 Cloverfield Blvd. Santa Monica, California 90404

79 06 11 054

ARPA ORDER NO. 3099

PROGRAM CODE NO. 6F10

DNA RMSS CODE B2270 76863
M99QAXYX91229

NAME OF CONTRACTOR: Pacific-Sierra
Research Corporation

AMOUNT OF CONTRACT: $295,827.00

CONTRACT NO. DNA001-76-C-0078

PRINCIPAL INVESTIGATOR: Frank J. Thomas
Phone No. (213) 828-7461

SHORT TITLE OF WORK: Effect of Burial
Depth on Seismic Signals

PREFACE

The program reported herein was a joint effort between Pacific-Sierra Research Corporation (PSR) and Applied Theory, Inc. (ATI). This report distills only the positive results of the calculational program in support of Test Ban Treaty verification and does not discuss the many efforts that were unfruitful. The authors would like to thank their many colleagues at PSR and ATI who contributed to the program; to Drs. D. Harkrider and E. Herrin, who provided valuable insight into the problem; and to Dr. C. Romney and Colonel G. Bulin at ARPA/NMRO, who helped keep us on track.

This is the first of two volumes reporting on work performed under contract to the Defense Advanced Research Projects Agency from October 1975 through November 1978. This volume contains the executive summary and main body of the report. Volume II contains the supporting appendices.

EXECUTIVE SUMMARY

This report discusses a calculational program aimed at improving U.S. capability to verify a Threshold Test Ban Treaty (TTBT) by seismic means.

The Soviets, in their PNE and weapon programs, may conduct nuclear tests at shallower depths than the United States or the French experience. Since yield estimation is thus required at depths for which little or no direct seismic data are available, we emphasize shallow bursts in our analysis and examine both body-wave and surface-wave effects.

Two-dimensional inelastic source calculations, using Applied Theory's AFTON program, were made on a representative set of 150-KT explosions. This set covers a range of depths and materials that might be used in Soviet weapon and PNE programs. These sources were used to develop synthetic seismometer body-wave signals at teleseismic distances. Considerable effort was devoted to excluding nonpropagating waves from the source description.

Simple elastic theory indicates that the primary body wave from a buried explosion receives positive or negative reinforcement from the free-surface reflection--the pP wave. The amplitude and direction of the reinforcement depend on timing, and therefore on depth of burial of the explosion. Our more refined calculations, which include inelastic and gravitational effects, indicate a "reflection" amplitude smaller than that calculated for the elastic case. More important, the reflected wave is relatively delayed in time, so that transitions between positive and negative reinforcement occur at shallower depths of burial--depths usable by the Soviets and therefore of crucial importance in verification of a 150-KT TTBT. Using the conventional m_b definitions and the AFTAC instrument corrections, we find the depth of burst varies with m_b by at least ± 0.2 in the 150-KT range.

The surface-wave model developed is based on Green's function. Many problems were encountered in modifying the AFTON source-data program to provide an input that was accurate for long-period displacements--

and to extrapolate data well beyond the reasonable truncation times for the program.

Though additional calculations must still be performed, our investigation has yielded the following preliminary conclusions:

1. For yield determinations and comparisons, inelastic effects (including cracking) and gravitational effects must be included in the analysis of either body waves or surface waves from shallow explosions.

2. For relatively shallow explosions (say, <1500 m at 150 KT), burial depth significantly affects both the body-wave and surface-wave signals. This effect has implications for earthquake/explosion discrimination as well as yield estimation.

3. Without correction for depth effects due to cracking and gravity, m_b (as conventionally defined) can result in systematic yield overestimation of shallow Soviet explosions in the 150-KT range in sedimentary rocks.

4. For burial depths between 200 m and 1500 m, covering the range of greatest interest for TTBT verification, the body-wave yield estimates may be improved by using uncorrected seismometer amplitude (A) from the first displacement swing, or from the largest displacement swing, or both--rather than a combination (conventionally found in m_b) of the largest amplitude with its associated period (T) and instrument correction. Use of A, alone and uncorrected, also appears to make m_b a more direct measure of radiated energy. Seismic data from selected explosions should be reexamined from this viewpoint.

5. Topography near the shot point does not appear to be a major factor in seismic signal generation.

Regarding conclusion 4: For modern seismometers, output amplitude is nearly proportional to the speed of ground motion between 1 Hz

and 3 Hz, the frequencies of greatest interest for explosion monitoring. Thus, the approximate logarithmic proportionalities:

$$\log (\text{seismometer-amplitude}) \sim \log (\text{ground-velocity}) \sim \log (\text{ground-velocity})^2.$$

The logarithm of the largest interval spanned by peaks and troughs of ground velocity is roughly proportional to the logarithm of radiated kinetic energy (and total radiated energy)--and so, therefore, is log (A). On the other hand, at the frequencies in question, A/T represents ground acceleration, which is not fundamentally related to radiated energy.

A generalized method for combining body-wave, surface-wave, and other measurements to refine yield estimates has been reported previously.[*]

Summaries of the body-wave and surface-wave calculations to date are presented in the body of this report. The appendices include additional details and numerical methods.

---

[*] A. Ciervo, et al., PSR Notes 91, 93, 113, and 122.

CONTENTS

FIGURES

xiii

TABLES

I. THE PROGRAM OF COMPUTATION

The main goal of the program reported herein was to determine, more accurately than before, how teleseismic surface and body waves driven by buried explosions vary with shot depth. At first, emphasis fell on shallow Soviet PNEs, and the scope of effort later widened.

A computer code (AFTON 2A) for calculating fields of axisymmetric continuum motion was the key tool used to define the ground motions studied. Since actual depths of burial seldom exceed a kilometer (km), and many buried bursts have produced craters, it was necessary in our computational work to take account of tensile cracking and gravity.

SCOPE OF THE COMPUTATIONAL PROGRAM

At the outset, we hoped to compute fields of motion for 18 buried bursts. Early on, that number was reduced to 12 when it was found that inelastic processes (mainly cracking with gravity) lengthened by at least a factor of two the time of significant motion in the near field (i.e., within a few kilometers of the shot point for bursts yielding 150 kilotons (KT) of energy). The hypothetical host media for the 12 bursts--each of 150-KT yield--were Piledriver granite (3 shot depths), wet sandstone (5 depths), dry sandstone (3 depths), and weak dry sandstone (1 depth).

Granite and sandstone were chosen as types of material in which Soviet PNEs would be likely to occur. Degree of saturation, a key property of earth media that affects both strength and compactibility, was varied (from 0% to 100%) in the change from wet sandstone to dry. Shear strength, another key property, was also varied; its effects on ground motion due to PNEs were explored via the change from dry sandstone to weak dry sandstone. Similarly, the effects of a variation in dry porosity alone (from 10% to 0%) are seen in the fields computed for weak dry sandstone and wet sandstone, whose strengths were identical.

The 12 bursts covered 5 different depths, viz., (10, 30, 39, 47.622, and 100) x $W^{1/3}$ meters (m), where W is the yield in kilotons. Containment was expected only for the depth 100 $W^{1/3}$, and shots at depths of 10 $W^{1/3}$ and 100 $W^{1/3}$ m were simulated only in wet sandstone. Also, since $30 \times 4^{1/3} = 47.622$, the 150-KT field for depth $30 \times 150^{1/3}$ m is a given

medium provided a simply scaled version of ground motion from a 600-KT burst at depth 47.622 x $150^{1/3}$ m. That 600-KT field could be compared with the 150-KT field computed for the same depth (47.622 x $150^{1/3}$ m). A similar comparison was possible between 37.5-KT and 150-KT shots at a depth of 30 x $150^{1/3}$ m. In addition, to assess gravity-caused departures from simple scaling rules, a calculation was made of motion for a yield of 600 KT at a depth of 30 $W^{1/3}$ m. Then, as interest in Soviet test-media grew, results obtained in another program for shots in a "Soviet granite" were augmented by three further calculations for that medium--two at depths other than the five already noted. Most important, at the very end of the program, motion was computed for a 150-KT shot at a depth of 744 m in wet sandstone. (Table 1 summarizes the full problem set.)

The last calculation cited was one of a series of nine, made necessary by results that surfaced at a late stage of the program. The nine final calculations were made after modifying the AFTON-2A code somewhat, in ways that improved its accuracy and thereby made it possible to determine ground motion at greater depths and later times than before. Besides the shot 744 m deep in wet sandstone, the final series included calculations of motion for the three granite bursts of Table 1, and the two in wet sandstone at depths of 39 $W^{1/3}$ and 100 $W^{1/3}$ (207.2 m and 531 m)--all five of which had been run earlier. Moreover, each of the three wet-sandstone problems of the final series was run twice: once with gravity and cracking; once without.

The motivation for the final nine-problem series, and the code modifications that preceded it, are discussed below. Here, we note that relative values of body-wave magnitude (m_b) originally obtained for granite changed by no more than 0.03; for the two recomputed wet-sandstone bursts, relative m_b-values changed by 0.22--but only because of slight differences in seismometer response that bridged an m_b-discontinuity (see Sec. III).

CRATERING CALCULATIONS AND THEIR SIGNIFICANCE

In the past, the dimensions of craters calculated for nuclear surface bursts using codes like AFTON 2A have been smaller by factors of 10 to 50 than observations of actual craters suggest. Yet, it is also true that the codes predict realistic craters for buried explosions [1] even when

Table 1

CALCULATIONAL MATRIX: TAMPED 150-KT EXPLOSIONS

Depth of Burial (m)	Material					
	NTS Granite	Dry Sandstone	Weak Dry Sandstone	Wet Sandstone	Soviet Granite
53.1 $10 \ W^{1/3}$				X	
159.4 $30 \ W^{1/3}$	X	X	X	X	X
207.2 $39 \ W^{1/3}$	X	X		X	
253.0 $47.622 \ W^{1/3}$	X	X		X	
401.7 $75.6 \ W^{1/3}$					X
531.3 $100 \ W^{1/3}$				X	
743.9 $140 \ W^{1/3}$				X	
1000.0 $188.2 \ W^{1/3}$					X

shot points are much shallower than the depths of interest herein (>50 m for 150 KT). Those results are explained, at least in part, by the simplicity of the process of coupling explosive energy to the ground, when shot depths exceed ∿3 m (for 150 KT). Also, unless shot depths are large (on the order of 1 km for a 150-KT burst), elastic tensile stresses above the shot point so greatly exceed strength limits that, to predict cracking, little detailed knowledge is needed either of tensile strengths or of cracking mechanisms. Accordingly, as an important result of our cratering-burst calculations, we were able to show that an adequate account of the effects of cracking and gravity is given by AFTON 2A. Specifically, the volume of our calculated Sedan Crater was 60-percent greater than that observed (versus error-factors of 10 to 50 for surface bursts); and, for granite and wet sandstone, our calculated dependence of crater size on shot depth was consistent with observation.

The ability to compute crater sizes was comforting, but insufficient, to secure the main goal of the program. Rather, our toughest computational problems arose from a need to define fields of motion at much later times (>2 sec for 150-KT bursts) than those to which explosion calculations are usually run; by contrast, for buried explosions, crater dimensions are largely determined by the early history of ground velocity (≤0.5 sec for 150-KT bursts in granite and wet sandstone).

THE NEED FOR CALCULATION TO LATE PROBLEM-TIMES: SURFACE WAVES

At about the time that the last of the program's three one-year phases began, a major result emerged: Surface-wave magnitudes were found to be roughly proportional to the logarithm of the net downward impulse delivered by an explosive source to the earth (Sec. II). More precisely, the critical quantity proved to be the vertical impulse delivered to the earth, in a few tens of seconds, across any surface S in the elastic near-field of the burst--provided that the shot point is enclosed by S-plus-the-ground-surface. The surface S was taken as a hemisphere H, viz., the lower half of a sphere with its center at ground zero, and having about the smallest radius consistent with elastic deformation (∿1.2 km for wet sandstone and 2.1 km for granite).

Apart from in-flight ejecta for the shallowest shot depths studied, all significant motion of material originally within the surface H ended before 10 sec--from which it follows that the vertical impulse delivered

across H in 10 sec is zero. Unfortunately, in all finite-difference or finite-element codes, the use of discrete analogs of the exact equations of motion to effect their numerical integration is attended by discretization error. As a result, the vertical impulse found from our first calculations was not exactly zero; that spurious impulse, though small in terms of the discretization error required to produce it, dominated our first values of surface-wave magnitude, M_s.

For our purposes, the net effect of discretization error was to impart a nonphysical acceleration of ~ 0.002 g to ground material in our "static equilibrium" fields (g $\equiv$ gravitational acceleration). In most applications, an error of that size would be negligible; in the present context it was unacceptably large. Translated into vertical displacement, for example, it amounted to about 6 centimeters (cm) after 2.5 sec of motion (the final time of most of our calculations); by comparison, the peak displacement for wet sandstone was ~ 24 cm at the bottom of the hemisphere H. Thus, the error was big enough to affect slightly the first values computed for m_b, although it was serious only for M_s. As discussed below, however, it became critical for m_b as well, when, late in the program, new facts came to light as to the properties of elastic near-fields. In the end, to compute surface- and body-wave fields reliably enough for this program, the simplest course was to eliminate the error entirely (see pp. 7-8). That was done, and 5 of our original 12 problems were then rerun; a new one was also run.

SPECIAL ACCURACY REQUIREMENTS IN COMPUTING BODY WAVES

A major result of our first calculations above was the discovery that ground displacements, as seen near the bottom of the hemisphere, H, varied greatly with depth of burial. They were also much different in their late stages (after ~ 1 sec of motion) than we were led to expect on the basis of (inexact) elastic half-space theory. Further, the duration and timing of surprising displacement-pulse features were such that tensile cracking (which was widespread, according to the calculations), and gravitational subsidence of the cracked medium, could have produced them.

In late 1977, the approximate picture of elastic near-field motion previously available gave way to a more accurate one, whose development

must be counted a major advance in the understanding of elastic near-fields (surprisingly) [2]:[*] The exact near-field of a compressive, burst-like point-source in an elastic half-space was derived (or rederived [3][**]). Thus, early in 1978, we learned that late-time, near-field displacements similar to those seen in our calculations would occur even in a gravity-free, uncrackable elastic medium. Furthermore, those elastic displacements would decay so rapidly with distance from the shot point as not to affect teleseismic body waves; they are "local parts" of the complete near-field. More precisely, drawing on the principle of superposition, the parts of a linear near-field whose absence would leave the far field unaffected, are referred to below as "local"; the part of the near field that cannot be altered without changing the far field is called "global."

The new knowledge of elastic near-fields plainly made it necessary to distinguish between elastic contributions to our calculated near-field displacements and all other contributions. In short, our key task became that of determining, as a function of burial depth, the influence on teleseismic body waves of processes not amenable to simple theoretical treatment--particularly, cracking and gravitational subsidence.

To separate elastic displacements from all others in the near-field of a given burst, we found it easiest to perform two calculations that were identical, except for the inclusion of gravitational acceleration and cracking in one of them, and not in the other. In both instances (since body-wave fields are irrotational), only the irrotational part of each near-field displacement pulse was wanted. That requirement, given available computational tools, was best met by calculating motion at much

---

[*] The effect of local terms on elastic near-fields was recognized first by S. Day (T. Bache; telephone discussion in October or November 1977). A check of the perfect-reflection approximation (Sec. III) against an exact solution was called for on 7 March and 8 August 1977 by J. Trulio (at NMRO-sponsored meetings), who suggested that an S^3 elastic-wave-propagation code be used to get it (analytic methods were used instead).

[**] Reference 3 is based on a solution to the problem of a compressive (spherical) time-varying source in a half-space due to L. Cagniard, in the translation of Flynn and Dix (*Reflection and Refraction of Progressive Seismic Waves*, McGraw-Hill, 1962) as corrected by J. Workman. Although surface waves are omitted, the results in AFSWC-TR-68-27 are virtually indistinguishable from the complete exact solution at steep takeoff angles, at least on the hemisphere H (and below).

greater depths than in the past. Shear and surface waves were thereby removed from the displacement pulses that define explosions as sources of teleseismic signals, simply because these waves travel too slowly to contribute to the first few seconds of deep near-field motion.

To obtain displacement pulses deep in the ground, motion had to be computed to even later problem-times than before (>3 sec, it was found). Hence, as in characterizing buried bursts as sources of teleseismic surface waves, forces again had to be in exact equilibrium in the static AFTON-2A field. For example, at the relatively great depths reached in our final calculations (∿6 km), peak displacements were only ∿2 cm, whereas a discretization error of 0.002 g in acceleration would have altered late-time displacements by 10 cm.

A computer code was available during the program that was supposed to propagate body waves correctly to teleseismic distances, starting from the hemispherical near-field surface H, even if the global part of the irrotational field came mixed with its local parts, and with shear and surface waves. However, the effects of cracking and gravity on near-field motion, free of shear and surface waves, and largely free of local contributions, could only be determined by calculating the near-field at great depths and late times. To do so, it was necessary to push the computational art forward a bit, as described below. When that was done, we found that the large effects on body waves attributed earlier to gravity and cracking, both in the near field of a buried burst teleseismically, remained large (Sec. III).

INNOVATION

The unique flexibility of the AFTON-2A code makes it practical to compute motion from a 150-KT explosion, without assumptions of small displacement, linearity, etc., and to depths as great as 6 km and times longer than 3 sec. Specifically, a domain of AFTON-2A computation can be held fixed in size while being moved continually downward at the speed of longitudinal waves. The cost of advancing a numerical solution through unit time is then constant, and the total cost of computation is proportional to the time after burst at which calculation is stopped. On the other hand, if all disturbed material had to be included in the

computational domain (usual with computer codes), then the cost of calculation would increase roughly as the cube of a final time of calculation, rather than the first power.

To achieve exact static equilibrium in a discrete field proved more difficult than to avoid excessive computation. As part of the overall discretization process, a continuous medium is divided into finite polyhedral cells of material, whose vertices form a "finite difference mesh" [4]. By adopting a simple approximation to the structure of an exact continuum field within a cell, discrete equations of motions are produced. The properties of those equations--and particularly the absence of properties not possible for a physical continuum--depend on the local (cell-scale) field-structure assumed. The properties of the discrete equations can be made completely consistent with those of the continuum equations they replace, but only if stress and strain are locally homogeneous (for reasons that, though not complicated, would take us too far afield to present here).

Some of the unique and basic transformation properties of the AFTON equations of motion--which include exact conservation of mass, momentum, and energy--are tied to the assumption of homogeneous strain and stress fields within cells. On the other hand, overburden stresses in a static equilibrium field (under gravity) increase continuously with depth. Those two different field-structures in the AFTON equations were reconciled-- but the effort was not trivial. Specifically, while preserving all transformation properties of the AFTON equations, as well as the nearly complete freedom of spatial mesh-point distribution offered by AFTON 2A, the code has now been modified so that its gravitational and material forces cancel exactly in static-equilibrium fields. So modified, the code was used to recompute the three granite fields studied in the program, and two of the original wet-sandstone fields (pp. 1-2, above). Also for wet sandstone, motion was computed for one new shot depth, and fields were calculated for the last three explosive-sandstone systems both with and without cracking and gravity.

II. SURFACE WAVES

INTRODUCTION

The PSR M_s model is based on Harkrider's analytic expressions for surface-wave Green's functions in a flat multilayered half-space [5]. The multilayer model of the earth structure is adopted because the modelled explosion sources with which we are concerned here all have cylindrical symmetry, and the symmetry of the layered earth model is also cylindrical.

Previous efforts by S^3 (Systems, Science and Software [6]) to calculate M_s from the same source model failed partly because of the difficulty in finding an equivalent point-source term for use with the whole-space Green's function. In fact, there is no equivalent point-source term, because the entire free surface becomes a source when whole-space Green's functions are used. The PSR M_s model uses half-space Green's functions and therefore avoids the source terms from the free surface. This method results in a source that is localized near the explosion and therefore easier to treat mathematically.

The following equation used to calculate M_s, derived from Marshall and Basham [7], is dependent only on the maximum vertical ground displacement near the 20-sec periods at a distance of 10,000 km:

$$M_s = 9.2 + \log (U_{max}[cm]) \quad . \tag{1}$$

The constant 9.2 has the distance and period correction already included according to the prescription in Ref. 7. The value of U_{max} is taken to be the maximum displacement from equilibrium in either the positive or negative direction.

The following discussion of the PSR M_s model is directed toward a complete specification of the source parameters used, followed by a description of the propagation method of calculating U_{max} for sources of interest. Note that this model calculation makes several simplifying physical assumptions, which are discussed briefly as necessary.

SOURCE MODEL

The following details of the nonelastic source model constitute a mathematical description of the source suitable for computing surface-wave magnitudes. Basically, we are dealing with a two-dimensional problem, since the theoretical problem of a spherical explosion in a homogeneous isotropic half-space has cylindrical symmetry. The plastic-flow character of the source need never enter into the description of the source vis-a-vis surface-wave creation. The volume of space where plastic flow and all other nonelastic behavior takes place can be surrounded by an imaginary surface outside of which the usual equations for small-amplitude linear elastic-wave propagation are valid. By surrounding the source, only the specification of the dynamic state of stress for material in contact with the imaginary surface is relevant for the propagation calculation, and the details of rock mechanics, etc., which produced that dynamic state, are no longer needed in the source description. Of course, by following this source description, we could have sources that are not physically possible. The above definition of any particular source, however, will have certain average values that give clues to its faithfulness to physical reality; e.g., net vertical impulse should be zero. In practice, the imaginary surface on which the elastic source is specified has been a closed numerical grid of vertical cylindrical strips and horizontal annular strips, located about 2-km away from the shot point. At one point during this study, the imaginary surface was a circular arc that was rotated about the axis of symmetry to produce a hemisphere centered at ground zero. This hemisphere acquired the name "magic circle," which is still applied to the numerical grid although it is no longer strictly circular.

The complete mathematical specification of magic-circle data needed for a formal propagation calculation can be determined by looking at the wave equation as an initial value problem in the theory of partial differential equations. By analogy with the one-dimensional wave equation, the value of the scalar potential and its first derivative must be specified on the boundary point to completely determine the solution everywhere. The analogous boundary conditions for the source considered here are the values and derivatives of the potential over a two-dimensional surface embedded in three space dimensions and one time dimension. In practice,

we would have to specify the potential and its derivatives over the hemisphere for a long time duration. The PSR M_s model, however, is limited 1) because it uses force, not potentials; and 2) because derivatives are not used at all.

The source description currently in use is a collection of directed ring forces located on the hemisphere swept out by the magic circle and with time dependencies determined by the numerical results of the modelled explosions as calculated by Applied Theory, Inc. We adopt the simplified source model for two reasons: 1) the solution is much simpler to implement, since point-force Green's functions were found in the literature; 2) good test cases have not yet been developed for the purpose of checking even the simple solution, and so the more complicated one would be premature until such a testing ability is developed, since the simpler method may be verifiable for explosion sources.

It is possible to get some idea of the validity of using a collection of ring forces by trying to imagine what the actual elastic solution for the ring forces would be, compared to the continuous distributed force model. First, the singularity in stress near the ring force is nonphysical. But if one were to observe the motion at a distance from the rings about equal to the ring spacing, then it is easily imagined that the ring-force solution would begin to resemble the distributed-force solution, although the details would depend on interference effects between the rings. In particular, it seems that ring forces would radiate energy both inward and outward equally, at least locally, whereas distributed forces would radiate energy predominantly outward relative to the magic circle. Intuitively, one would expect that if the response due to the ring forces at a moderate distance outside the magic circle could be made by diffraction to resemble the distributed-force response, then the same diffractive effect would limit energy radiation inward as well. But even if diffraction effects did not operate as hoped, the energy budget would still not be off by a factor of more than two; and as long as the different explosions do not differ radically, which is the case, the relative values of M_s should still be meaningful.

Figure 1 represents the surface elements for a wet-sandstone grid on which the ring forces are defined. Note that the surface elements are all
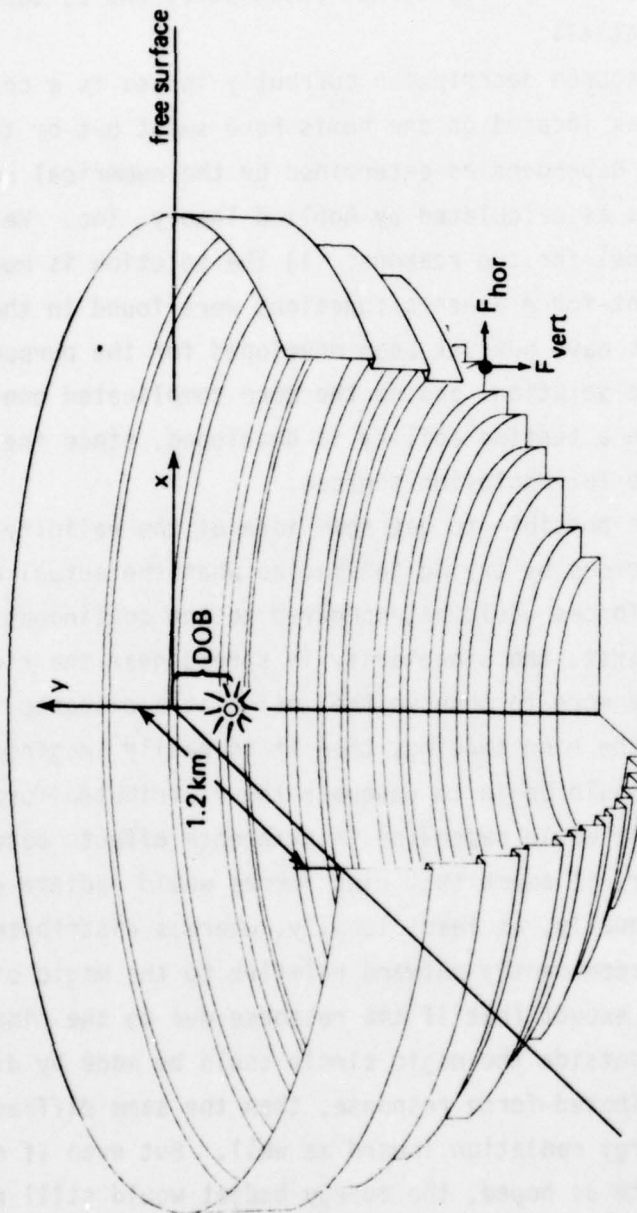
12

Fig. 1--Grid elements used to model magic-circle data of source volume for wet sandstone. Two force components are shown for one of the rings at one instant of time. DOB = depth of burial.

nearly vertical or nearly horizontal, but the direction of force on either does not have to align with the surface normal. There are typically about 60 directed force elements for each explosion event, and the time duration runs about 2 sec.

PROPAGATION MODEL

The basic element of the propagation model is the surface-wave Green's function that describes in one complex number the teleseismic vertical ground motion (amplitude and phase) when the source is a buried point force (horizontally or vertically directed) that has harmonic time dependence. Figure 2 represents what the Green's function does--which is to solve for the teleseismic vertical displacement due to one component of our model source. The solution for the complete source is found by superposition in time and space of the component parts.

The desired result is the vertical ground motion $U(t)$ (in centimeters) at a large but arbitrary range of 10,000 km as a function of time. Once this function is found, the maximum value, U_{max}, is used in Eq. (1) to give M_S. The full-time dependence is found in the usual way by Fourier synthesis of all component harmonic terms:

$$U(t) = \frac{1}{2\pi} \int_{-\infty}^{\infty} \tilde{U}(\omega) \, e^{i\omega t} \, d\omega \quad . \tag{2}$$

The Fourier transformed displacement, $\tilde{U}(\omega)$, depends on the source terms only at the angular frequency ω; but on the individual force elements located at all different positions on the magic circle. The teleseismic response $\tilde{U}_j(\omega)$ for the j-th ring force is a linear combination of both the horizontal and vertical components of the force element at the frequency ω, $P_{Vj}(\omega)$, and $P_{Hj}(\omega)$, multiplied by the horizontal and vertical ring-force Green's functions, $G_{Vj}(\omega)$ and $G_{Hj}(\omega)$:

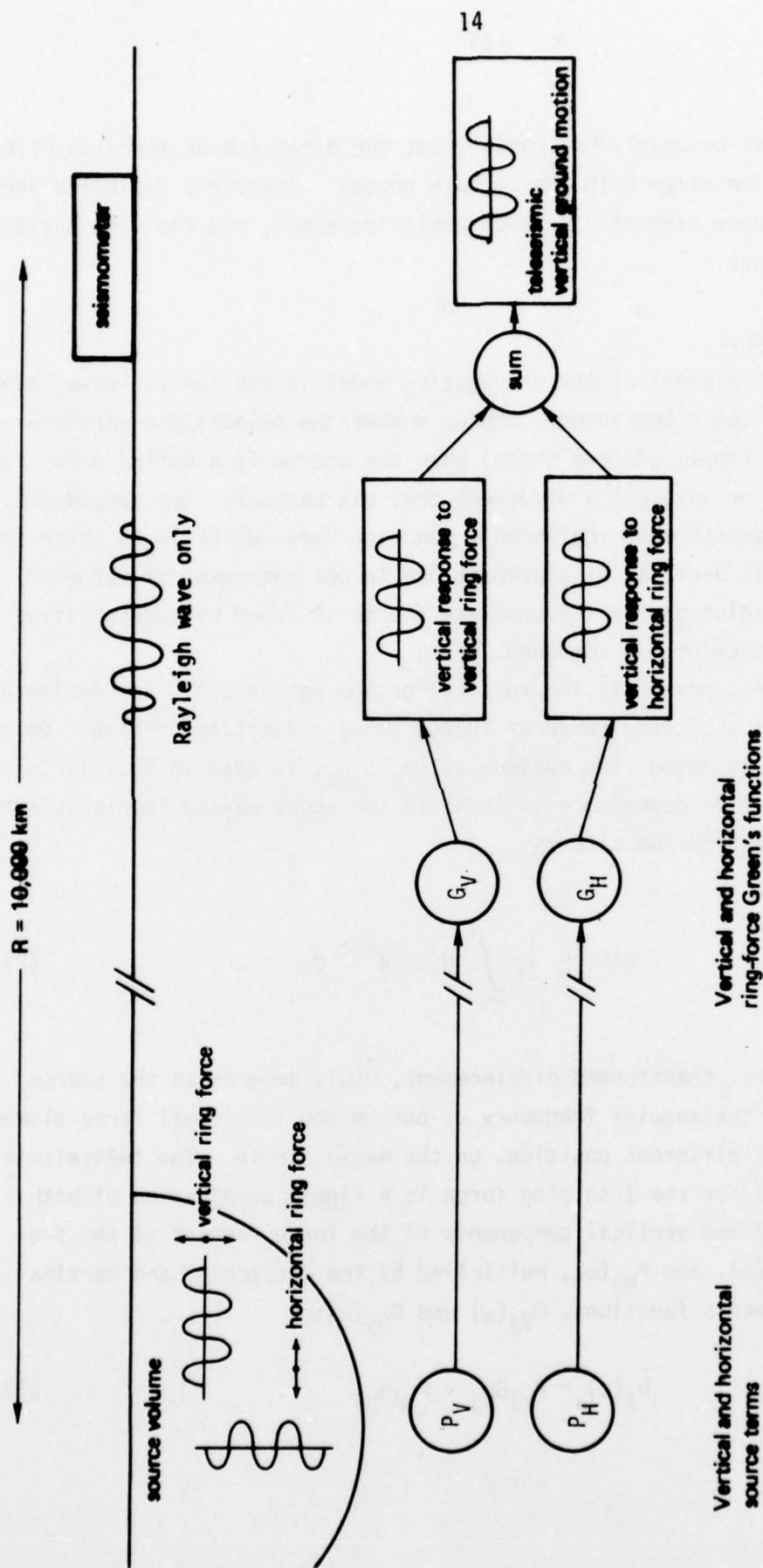$$\tilde{U}_j(\omega) = P_{Vj}G_{Vj} + P_{Hj}G_{Hj} \quad . \tag{3}$$

Fig. 2--Schematic outline of PSR M_s model showing source terms, propagators, and vertical response for one harmonic component and one ring force. Complete vertical response requires a summation over all rings and all harmonic components.

The force terms P_{Vj} and P_{Hj} are the Fourier components of each ring force at the angular frequency ω. In general, the time duration of the force for the simulated explosion events runs out to about 2 sec, whereas the frequencies of interest correspond to about 20-sec periods. Since any finite pulse has all frequency components included, the individual 2-sec force pulses will have 20-sec components as well, but of very small amplitude. At first, one is tempted to assume that $e^{i\omega t}$ changes so little for $0 < t < 2$ sec for ω corresponding to 20-sec periods that the 20-sec component is nearly the same as the "zero-frequency" component. In general, that would be a good approximation. But for the particular mechanical situation here, the conservation-of-momentum principle requires that the net vertical impulse transmitted by the magic circle should be equal to zero. Therefore the sum over all vertical force elements has a zero frequency component equal to zero:

$$\left\{ \sum_j P_{Vj}(\omega) \right\} \Bigg|_{\omega=0} = 0 \quad . \tag{4}$$

In practice, Eq. (4) is beyond the range of the modelled sources because the lowest frequencies are not strictly zero, but instead correspond to 2-sec time periods; and at those periods, the conservation of momentum applied at the magic circle is affected by ejecta that may still be in freefall for some explosion events.

We therefore must be somewhat cautious in using the small-phase approximation for $e^{-i\omega t}$, since we know the 20-sec component and the zero-frequency component of the total vertical impulse are not equal. In the propagation calculation, we have adopted the small-phase approximation, and have forced Eq. (4) to be satisfied by modifying the magic-circle data in a simple manner that simulated the effect of all returning ejecta.

The last piece to the outline of the propagation calculation is the pair of ring-force Green's functions G_{Vj} and G_{Hj}. The force functions are calculated from the point-force Green's functions g_V and g_H of Ref. 5 for the harmonic-force components, corresponding to the depth and radius of the j-th ring force of the magic circle. The ring functions G_V and G_H are found from the point functions g_V and g_H by integration of the point-force density per radian over a complete circle of the azimuth angle.

Note that all contributions of the azimuthal integration are additive for the vertical force, but there is cancellation on opposite sides of the circle for the horizontal force. This cancellation results in a ratio G_H/G_V, which is reduced from the ratio g_H/g_V by a factor of about $\pi r/\lambda$, where r is the radius of the ring (≈ 1 km) and λ is the Rayleigh wavelength (≈ 60 km).

The point-force Green's functions used here differ from those of Harkrider [5] in two relatively minor ways. First, the actual multilayered Green's functions are replaced by an approximation in which both the amplitude and the depth dependence are adjusted for each frequency so that it looks like a homogeneous half-space Rayleigh wave. This adjustment makes use of the dispersion relation for the multilayered half-space, but it avoids the necessity of doing the full multilayered calculation once the dispersion relation is known. The dispersion relation published by McEvilly [8] for North America is used here. Second, an amplitude-damping model is added so that a better estimate of absolute value of M_s can be obtained, although it is still felt that relative values of M_s are more meaningful. The damping model uses a constant Q damping factor, where Q is defined as the inverse of the fractional energy lost per cycle of a wavetrain. The justification for a constant Q model is given by Knopoff [9]; and the value Q = 300, which is used in this model, represents a compromise between values suggested by Knopoff (Q = 150) and Tryggvason [10] (Q = 1300).

RESULTS

Results presented in this section are of three basic types: 1) the M_s versus depth results of the physical model; 2) a sensitivity study of the effects of changing a few numerical parameters on the last data frame of the time sequence; 3) an identification of relevant source parameters that correlate strongly with M_s.

Figure 3 and Table 2 show the M_s versus depth results for the nine explosion events studied. Of the nine, all three shots in granite resulted in craters, whereas only the shallowest one in wet sandstone cratered. The shallowest one in "elastic" wet sandstone would have cratered had not the material been artifically prevented from failing in tension. Table 2 shows a list of results, including cratering, for the shots studied.
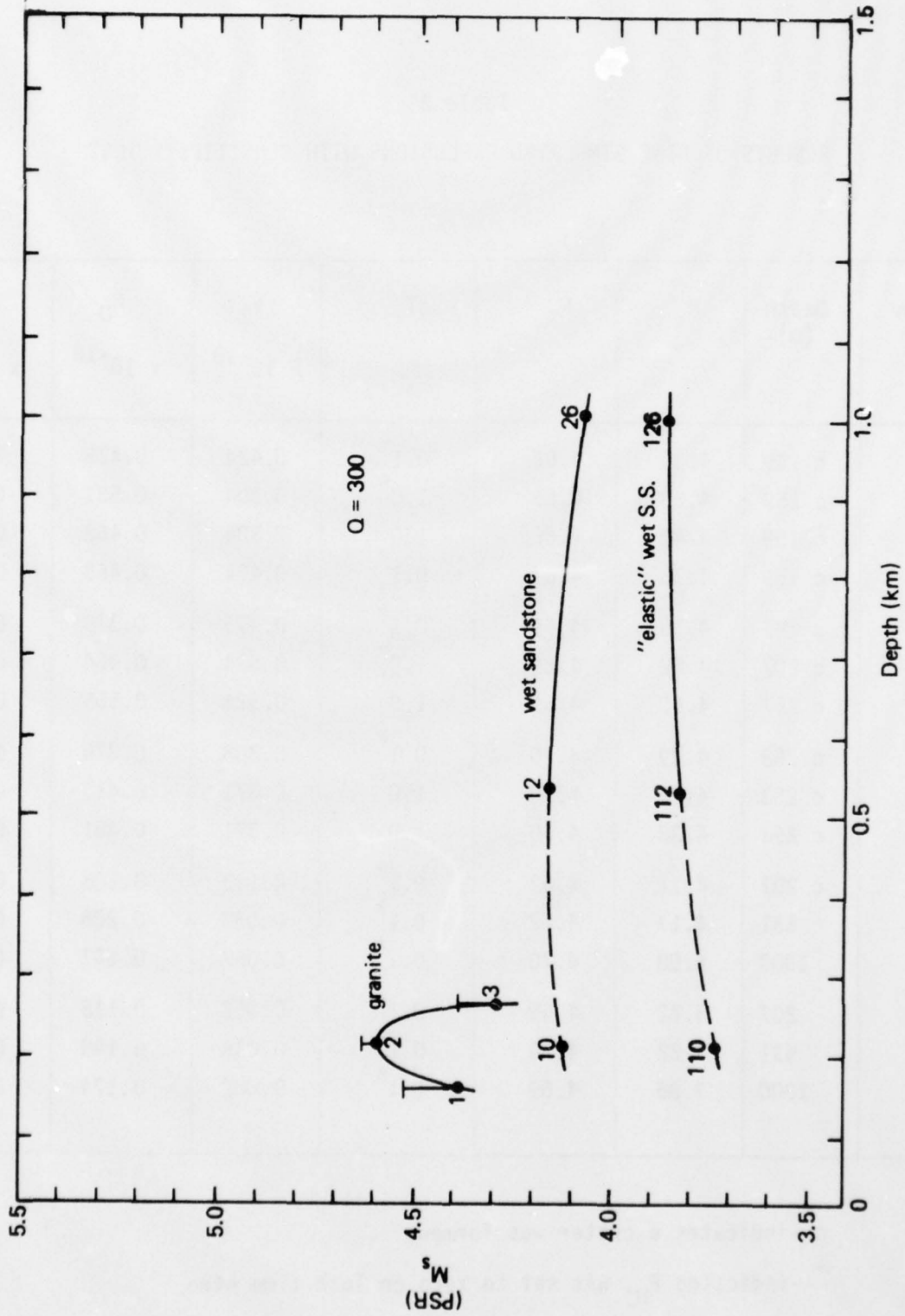
Fig. 3--Surface-wave magnitude (M_s) versus depth of burial in granite and wet sandstone with an average earth-damping factor Q=300.

Table 2

RESULTS OF NINE SIMULATED EXPLOSIONS WITH SENSITIVITY TEST

Problem Number	Depth (m)	M_S	M_R	ΔT sec	V_1 x 10^{-18}	H_0 x 10^{-18}	M_2 x 10^{-18}
1a	c 159	4.38	4.66	0.1*	0.424	0.475	0.636
1b	c 159	4.52	4.66	1.0*	0.304	0.531	0.611
1c	c 159	4.40	4.66	1.0	0.304	0.468	0.558
1d	c 159	4.38	4.66	0.1	0.424	0.468	0.631
2a	c 207	4.59	4.69	0.1*	0.475	0.378	0.607
2b	c 207	4.62	4.69	1.0*	0.524	0.464	0.700
2c	c 207	4.60	4.69	1.0	0.524	0.558	0.765
3a	c 253	4.29	4.70	0.1*	0.308	0.378	0.488
3b	c 253	4.34	4.70	1.0*	0.371	0.413	0.555
3c	c 253	4.38	4.70	1.0	0.371	0.451	0.584
10	c 207	4.11	4.62	0.1*	0.142	0.108	0.178
12	531	4.17	4.67	0.1*	0.057	0.206	0.213
26	1000	4.08	4.70	0.1*	0.057	0.207	0.215
110	207	3.72	4.69	0.1*	0.052	0.115	0.126
112	531	3.82	4.70	0.1*	0.048	0.146	0.154
126	1000	3.86	4.69	0.1*	0.052	0.174	0.182

c--indicates a crater was formed.

*--indicates F_{Hj} was set to zero on last time step.

The surface-wave magnitude falls in the proper range for 150-KT explosion events when compared with a list of measured M_s versus yield values from 47 NTS events [11]. Of the 47 events, 4 had yields between 155 KT and 170 KT, with M_s values from 3.97 to 4.32. Our results for granite are on the high side of that distribution, but it is not known whether a granite shot is included in the NTS list.

The PSR M_s values for the granite shots as shown in Fig. 3 are all higher than the wet-sandstone values, but it is felt that this distinction does not have conclusive theoretical support, because M_s is calculated from force alone and not from both forces and displacements. Richter's [12] magnitude expression based on total transmitted energy--which is proportional to the log of the energy in ergs--is calculated for each of the explosion events and presented as M_R in Table 2. Because the energy output is about the same for both granite and sandstone media--but since granite has a larger modulus of rigidity--one would expect larger forces for granite. But because the rate of energy involves the product of force and rate of displacement (velocity) on the magic circle, one would expect larger displacements for sandstone. The model assumptions used are not able to preserve the above-mentioned distinction between the relative magnitudes of the force components for granite and sandstone. This distinction would require that a pure surface wave passing through the magic circle should conserve its energy, and therefore if granite forces were larger than sandstone forces on one side of the magic circle, the granite forces should also be larger on the other side. This requirement is not fulfilled, however, for the Green's function method used here, because the response is measured in centimeters of displacement per dyne of force, which means that the larger forces of granite will produce displacements that are larger than the sandstone values of displacement, contradicting the equivalent conclusion based on conservation of energy applied to the two media.

The above ambiguity of the model does not apply to the relative M_s values of different shots in the same medium. For granite, the variation of M_s is caused by changes in the shapes of the time-dependent forces acting on the magic circle, and not changes in medium parameters. The slight change in M_R as a function of depth indicates that some mechanism is withholding more energy at shallower depths, which probably represents energy required to form the crater and propel ejecta. The variation of

M_S values for granite suggests significant interaction with the free sur-
face, and also suggests that this interaction has a strong enough depth
dependence to cause a measurable (0.3 units) change in M_S.

Some confirmation is given to the M_S values for granite by the sensi-
tivity test, whose range of values is shown by the error bars in Fig. 3,
and which reveals that the overall shape of the granite curve is unchanged
if M_S is assumed to lie within the error bars.

The interpolated wet-sandstone curve of Fig. 3 shows no strong depth
effect, but the resolution of the data points in the region of cratering
(one point) is not enough to draw any conclusion. The two deep noncrater-
ing wet-sandstone shots have nearly the same M_S value, which is to be
expected according to simple elastic scaling as long as the depth is much
less than one Rayleigh wavelength.

The "elastic" wet-sandstone M_S values are all consistent with a reduced
interaction with the free surface, although *elastic* here refers only to
the absence of cracking and gravity. Generally, the higher values of M_S
for the nonelastic wet sandstone seem to be due to residual block motion
(a free-surface interaction) that prolongs the force-time histories and
allows more energy into the 20-sec period range. If one follows this line
of reasoning, the shallowest elastic wet-sandstone shot would have the
smallest M_S value because the significant interaction with the free surface
would be over with in a shorter time period and therefore would deposit
less energy in long-period components.

Next, all of the results presented in Table 2 and Fig. 3 are based on
time histories of force that were modified in a somewhat ad-hoc manner.
The original force-time histories were characterized by an initial sharp
pulse, followed by a rebound, some reflection arrivals, and then a tail
of low-intensity oscillating force. The cut-off point on the oscillating
tail would, in general, be at a time when the net vertical impulse was not
zero; and this small residual vertical impulse would dominate the spectral
amplitude near the 20-sec periods. Therefore, after about 2 sec, at the
end of simulation, one extra time step was added, with a resultant force
that, when applied for ΔT sec, would cause the net vertical impulse to be
zero. This extra force at the end is not completely specified by the
requirement, $V_0 = 0$, where

$$V_0 = \int_0^T F_V(t)\ dt \quad . \tag{5}$$

The unspecified parts are the *distribution* of the vertical force over the magic circle and the prescription for specifying the *horizontal* component. The distribution of the vertical component is taken to be uniform and the horizontal component is either set to zero everywhere or given the value of the previous time step. This choice is indicated on Table 2 (p. 18) by an asterisk (*) affixed to the value of ΔT when the horizontal component, F_H, is set to zero, and by no indication when the previous values of F_H are used. Table 2 shows various combinations of ΔT and F_H tried for granite. Only the combination $\Delta T = 0.1^*$ is used for wet sandstone. In either instance, the velocities for the last time step are set to zero, and so the total energy transmitted is not affected.

Of the various force values used on the artificial last step, all M_S values fall within the error bars shown on the granite curve of Fig. 3. The largest difference is for Problem 1, the shallowest shot, where M_S varied from 4.38 to 4.52, a difference of 0.14 units. Figure 4 shows some detailed time histories for Problem 1 for the case $\Delta T = 0.1^*$. Since the net vertical force (Fig. 4a) must integrate to zero, the spectral source amplitudes have a lowest-order dependence on V_1, where

$$V_1(T) = \int_0^T F_V(t) \cdot t\ dt \quad . \tag{6}$$

One can clearly see the artificial last 0.1 sec of vertical force emerge above the oscillating tail (Fig. 4a) to drive V_0 to zero at the end time. A more realistic force-time history would have involved two oppositely directed vertical-force components, one upward, due to buoyancy while the ejecta is in free fall; the other downward, due to small impact. The final value of V_1 would therefore depend on momentum carried by the spall and the periods of the different possible trajectories. The approximations
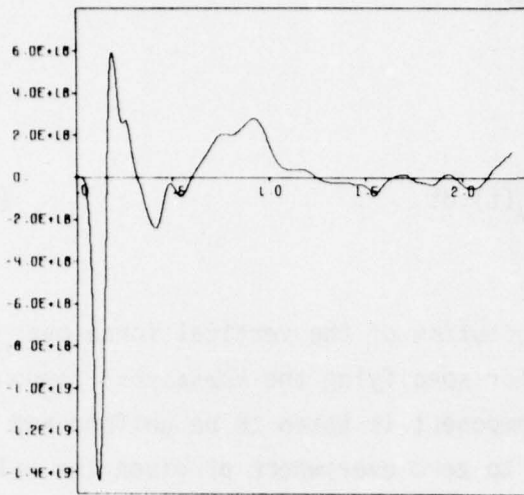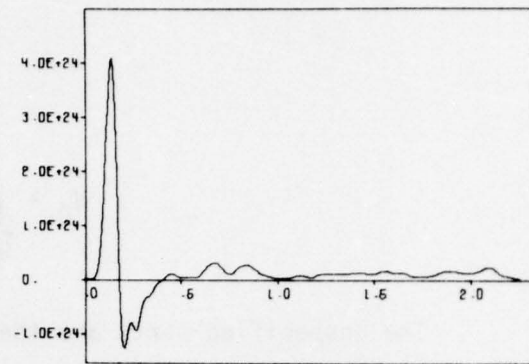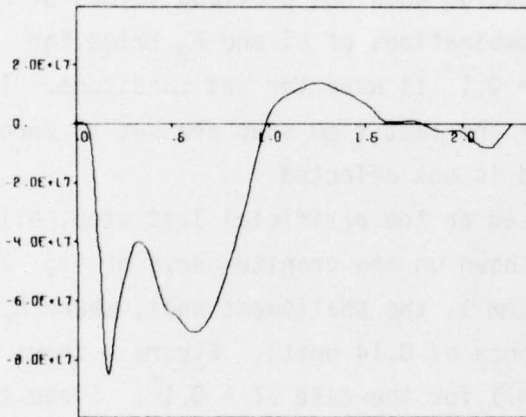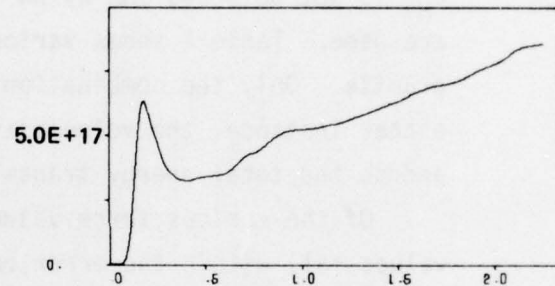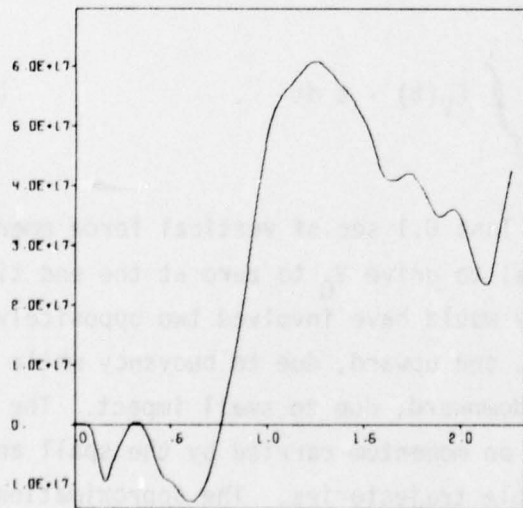
Fig. 4--Details of shallowest granite
simulation

a. Total vertical force versus time
b. Cumulative vertical impulse
   versus time
c. Cumulative first-time moment
   of vertical force versus time
d. Weighted horizontal force
   versus time
e. Cumulative horizontal impulse
   versus time

used here are still of value, however, because they show that various reasonable ways to terminate affect M_s less than the depth of burial (DOB) physical parameter.

The magnitude of the transient impulse due to ejecta was estimated to be about one-tenth the value due to spall for a typical cratering explosion [13], which gives a spall inpulse of about 10^{18} dyne-sec and an ejecta impulse of 10^{17} dyne-sec. These transients can be clearly seen in Fig. 4b, except some interpretation of the curve must be made because we see in the figure the reaction of the impulse on the rest of the world, and there seems to be some rebounding taking place. The value of V_0 at $T = 2.1$ sec, just before the last artificial time step, is about -10^{17} dyne-sec, which can be interpreted to be the downward impulse delivered to the world as the ejecta is thrown up. Additionally, the transient spall impulse is assumed to have died out.

With the above interpretations of the shape of Fig. 4b, we find good agreement between the estimated values for spall and ejecta impulse, and the numerical values on the figure.

From this point on, since the ejecta is in free fall, there should be a net upward force due to the lightening of the load removed by the free-falling ejecta, and this upward force would cause V_0 to increase positively in value, passing through zero and continuing upward until the ejecta falls back to earth, at which time V_0 returns to a value of zero. Since this imagined time history was not included in the source data, we do not know for certain how $V_1(t)$ (Fig. 4c) would be affected; but it is not expected to be greatly affected because of the results of the sensitivity analysis described above.

Finally, some results of a theoretical nature were found concerning the correlation of V_1 and H_0 with M_s, where

$$H_0 = \int_0^T F_H^*(t)\, dt \; ; \tag{7}$$

that is, H_0 is the zero-th time moment of the weighted horizontal force F_H^*. F_H^* is not the total horizontal force on the magic circle, because by symmetry that force must be zero at each instant of time. Instead, F_H^* is a measure of the surface-wave-producing ability of oppositely directed horizontal forces separated by a distance 2r. According to the source

calculations of the PSR M_s model, the resultant $F_H^*(t)$ is a summation over the individual ring sources as given by

$$F_H^*(t) = \sum_j \frac{X_j}{2C_R} F_{Hj}(t) \quad , \tag{8}$$

where X_j is the x-coordinate of the j-th ring force, and C_R is the Rayleigh-wave phase velocity for 20-sec period waves. One can easily see that H_0 and V_1 both have units of (dyne-sec^2).

In the full-blown propagation calculations, each $F_{Hj}(t)$ and each $F_{Vj}(t)$ enters into the seismometer response, with factors representing frequency and depth dependencies; but most of this dependence is only slowing changing, and can be factored out to a certain degree of approximation.

After this approximation is made, the result is that the M_s value is proportional to M_2, where the subscript 2 indicates that it is the coefficient of ω^2 in the spectral expansion of the teleseismic ground response, and where

$$M_2 = \sqrt{V_1^2 + H_0^2} \quad . \tag{9}$$

For the vertical moment V_1, it is clear that the net vertical force $F_V(t)$ must reach zero after some time period—say, after all ejecta have returned to earth. The formation of a cavity at the explosion site, however, has the effect of leaving a residual outward force $F_H^*(t)$ acting at the magic circle, and so $H_0(t)$ will continue to increase indefinitely with time, as can be seen in Figs. 4d and 4e. But since the time moments of the forces are used only as coefficients in the spectral expansion, we could always go back and replace the expansion by $\exp(-i\omega t)$, which would serve to cut off the artificial growth of the individual spectral components. For the present effort, however, the expansion must suffice.

Figure 5 shows a scatter plot of M_s versus M_2 for the entries in Table 2 (p. 18). Apparently, a quite good correlation exists between
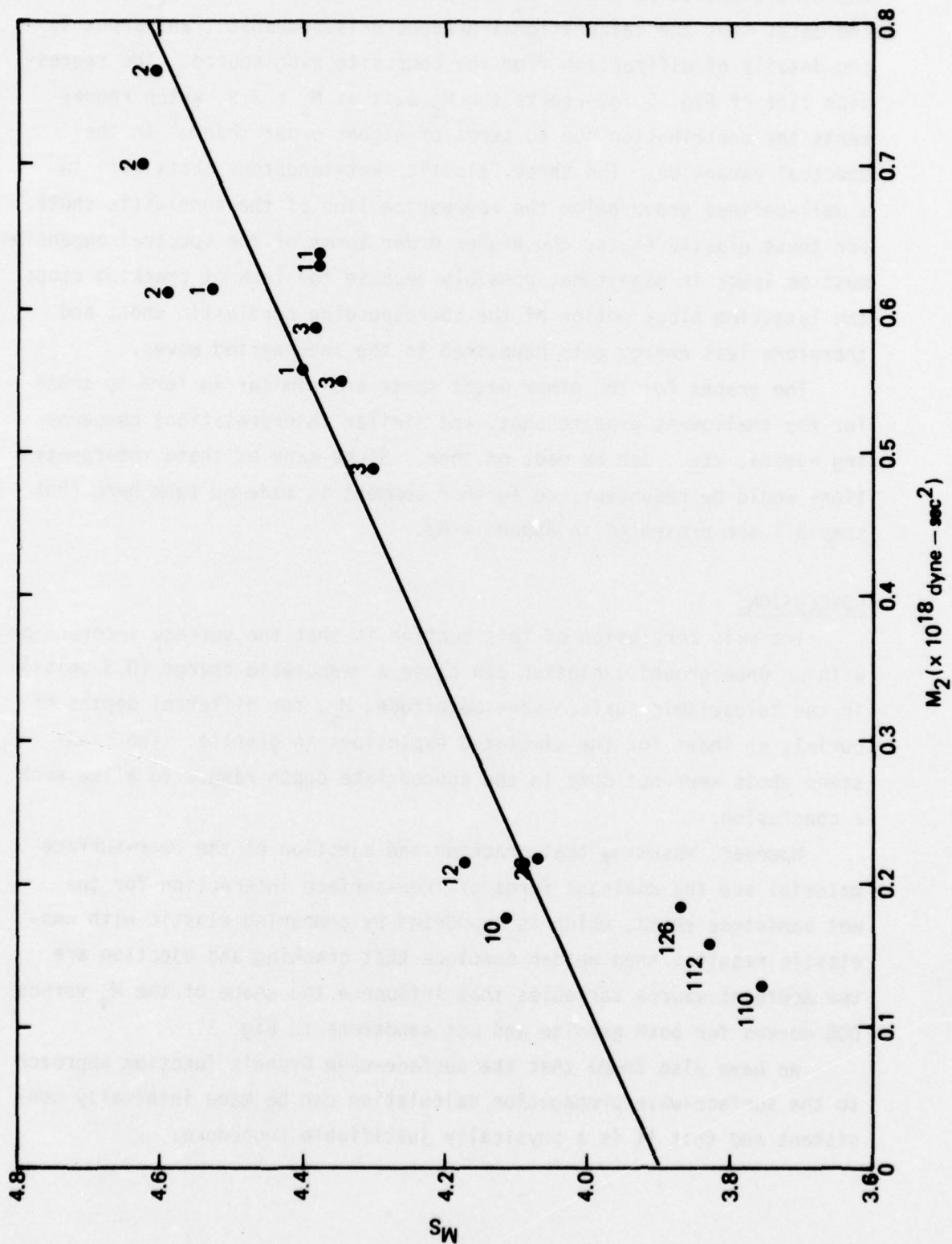
Fig. 5--Scatter plot of M_s versus M_2 for all entries in Table 2 (p. 18) showing a good correlation.

the single-source parameter M_2 and the resulting value of M_s, which indicates that the calculational procedure is somewhat transparent to the details of diffraction from the composite ring source. The regression line of Fig. 5 intersects the M_s axis at $M_s = 3.9$, which represents the contribution due to terms of higher order than ω^2 in the spectral expansion. The three "elastic" wet-sandstone shots fall in a well-defined group below the regression line of the nonelastic shots. For these elastic shots, the higher order terms of the spectral expansion must be lower in magnitude, possibly because the lack of cracking stops the late-time block motion of the corresponding nonelastic shots and therefore less energy gets deposited in the long-period waves.

The graphs for the other eight shots are similar in form to those for the shallowest granite shot, and similar interpretations concerning ejecta, etc., can be made on them. Since many of these interpretations would be redundant, no further comment is made on them here (but they all are presented in Appendix G).

CONCLUSIONS

The main conclusion of this section is that the surface interaction with an underground explosion can cause a measurable change (0.3 units) in the teleseismic surface-wave magnitude, M_s, for different depths of burial, at least for the simulated explosions in granite. The sandstone shots were not done in the appropriate depth ranges to allow such a conclusion.

However, assuming that cracking and ejection of the near-surface material are the dominant forms of free-surface interaction for the wet sandstone shots, which is supported by comparing elastic with non-elastic results, then we can conclude that cracking and ejection are the dominant source variables that influence the shape of the M_s versus DOB curves for both granite and wet sandstone in Fig. 3.

We have also found that the surface-wave Green's function approach to the surface-wave propagation calculation can be made internally consistent and that it is a physically justifiable procedure.

III. BODY WAVES

We have reached three main conclusions regarding the influence of burial depth on body waves:

1. Particularly as it influences the contribution of reflected waves to irrotational motion, burial depth must be taken into account in relating values of m_b to yield. In wet sandstone, m_b was found to vary by 0.38 (and, hence, estimated yield by a factor of 2.6 to 3.0) over the burial-depth-interval from 200m to 550m.

2. For depths >200m, magnitudes that are almost depth-independent can be obtained from the "b" phase of seismometer displacement; the role of such magnitudes (denoted "m_a") in yield estimation is at present minor, and should be enlarged.

3. If reflection is assumed to take place elastically at the ground surface, then estimates of the effects of burial depth on body waves emerge that are at most qualitatively correct. To compute the range of variation of m_b, or the depth-interval over which values of m_b span that range, we must take account of both gravity and tensile cracking on the motion of the medium.

Qualitatively, the first two of these conclusions are not new (e.g., see Ref. 14 and AFTAC-TR-77-37). Previously, however, they have been reached by assuming reflection to be elastic--a procedure that we find inadequate for quantitative purposes (conclusion 3).

BODY-WAVE MAGNITUDES VERSUS SHOT DEPTH: INTERACTION OF DIRECT AND RELATED WAVES

Conclusions 1, 2, and 3 above follow from Fig. 6. This figure contains both our computed m_b-values for inelastic reflection, and computed values that show how m_b would vary if tensile cracking and gravity were absent (semielastic reflection). Curve 3 in the figure refers to purely elastic reflection, treated approximately. As is
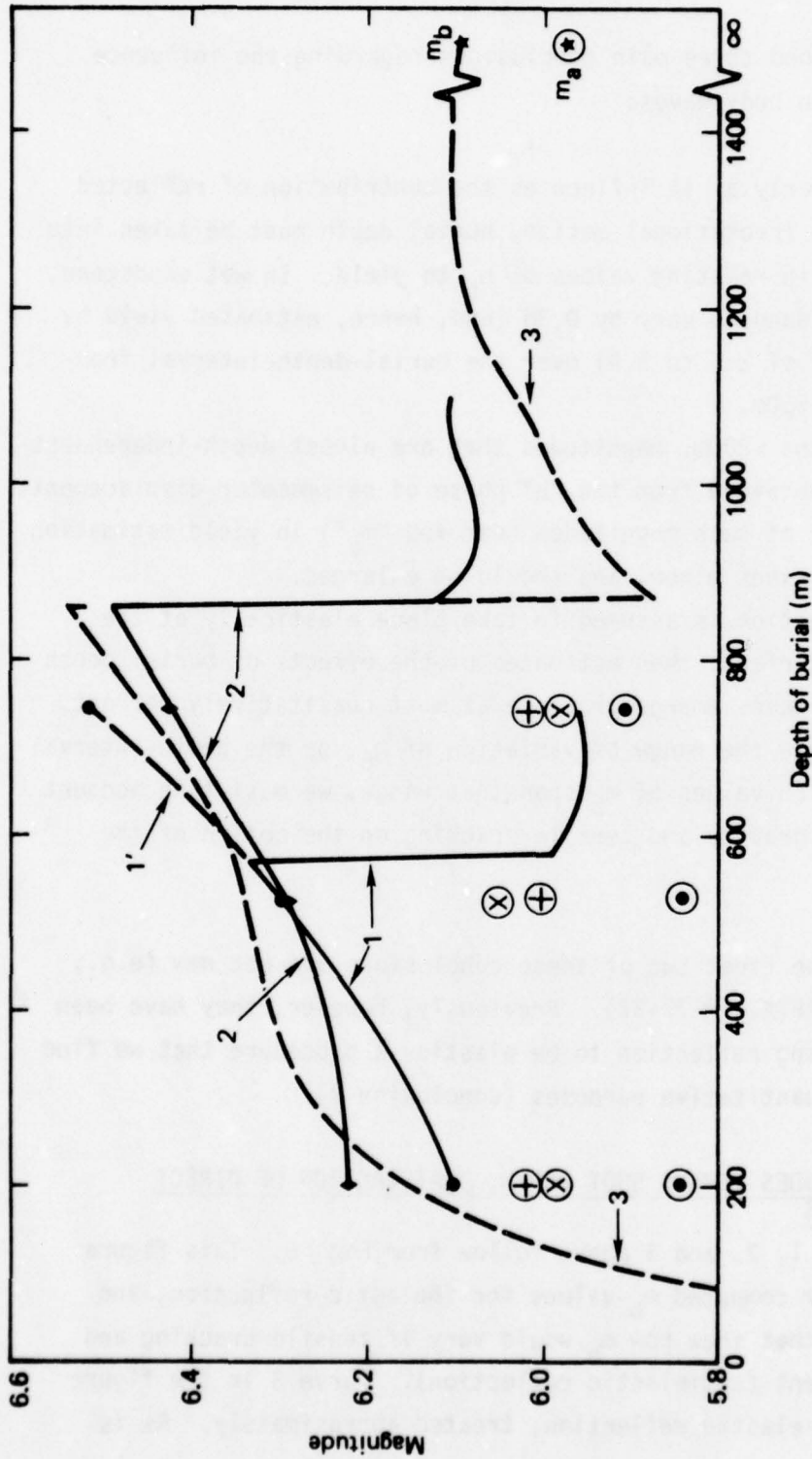
28

Fig. 6—Body-wave magnitude versus depth of burial, computed for 150 KT bursts in a wet-sandstone half-space. Curves 1, 1', 2, and 3 give values of m_b; points $\oplus$, $\otimes$, and $\odot$ denote m_a values. Gravitational forces and cracking are taken into account in calculating curves 1 and 1', but not curves 2 and 3. Reflection from the ground surface is treated as purely elastic, and by an approximate method, generating in curve 3. For curves 1, 2, and 3, each magnitude is derived from the first minimum and second maximum of a synthetic seismogram; the first minimum and largest subsequent maximum are used for curve 1'. Points $\odot$ came from the calculations that produced curves 1 and 1'; points $\oplus$ and $\otimes$, respectively, came from the calculations that produced curves 2 and 3.

evident from Fig. 6, m_b does not vary monotonically with burial depth in any of the three cases. Points obtained from phase b of our synthetic seismograms (m_a-values) also appear in Fig. 6; their relative independence of depth is clear.

The magnitudes of Fig. 6 are determined by the combined effects of two waves: 1) a nearly spherical (and initially compressive) wave driven away from the shot point by high pressures that attend explosive energy release; 2) a reflected wave (mainly expansive) due to relief of spherical-wave stresses at the ground surface. More precisely, for a 150-KT explosion at a given depth, the teleseismic body-wave-field manifested in Fig. 6 can be viewed as the sum of 1) a "direct" wave, defined as the wavetrain the burst would generate in a whole-space; and 2) a "relief" wave created by reflection of the direct wave from the ground surface. In deriving curve 3, the initial wave is taken as the field calculated for a burst in a uniform whole-space of wet sandstone, and the relief wave as its negative (implosive) image; the centers of the two wave-fields are separated by twice the depth of burial. In every other instance, both waves are generated as part of a complete numerical solution of the equations of motion.

For explosions at the ground surface, the direct wave and relief wave are produced at almost the same time, and hence largely cancel each other. As burial depth increases from zero, however, the relief wave begins to lag behind the direct wave (relief starts only after the direct wave reaches the ground surface), and the cancelling effects of one wave on the other diminish. At a still greater burial depth, the relief wave arrives just as the negative stage of direct-wave motion (i.e., motion back toward the shot point) ends. As a result, at points on nearly vertical downgoing rays, the passage of time is marked by a large, continuous change from downward to upward displacement; when thus in phase, the two waves reinforce each other. Ultimately, shot depths are reached when the relief wave lags so far behind the direct wave that the two no longer interact.

The effects noted have counterparts in seismometer response. Thus, as shot depth increases, m_b increases at first and then decreases, arriving finally at a whole-space value ($\sim$1250m for wet sandstone).

Before reaching its whole-space value, m_a also varies with burial depth.
Since m_a is determined by relatively early features of seismograms,
however, the relief wave ceases to have any effect on m_a at a depth of
burial ($\sim$820 for wet sandstone) and a lag-time that are relatively
small. For reasons noted below (p. 31), relief-wave effects on m_a are
much smaller than for m_b, from 820m to depths as shallow as 200m.

FURTHER COMMENTS ON FIG. 6: ELASTIC VERSUS INELASTIC REFLECTION

Separating the far field of a burst into a whole-space ("direct")
wave and a relief wave is convenient in that complete body waves re-
duce to direct waves at great burial depths. More important, for
bursts of a given yield, the separation in question assures that changes
in burial depth will affect the relief wave alone. In addition, given
elastic reflection, the shape and amplitude of the relief wave itself
become independent of burial depth in the far field. The teleseismic
body wave then depends on burial depth in one way only: the time by
which the relief wave lags behind the direct wave is proportional to
that depth.

More specifically, seismograms are affected by lag-time. Consider
first elastic near-field reflection. As shown teleseismically, dominant
periods in the direct displacement wave run from 2 sec to 3 sec (com-
ponents with shorter periods are damped relatively strongly by the
earth as they run from near-field to far-field). On the other hand,
the AFTAC seismometer is a narrow-band instrument most sensitive to
displacement harmonics with periods of $\sim$0.5 sec. The first forced
oscillation of the seismometer should therefore take place with a
period somewhat longer than 0.5 sec. Hence, as the relief wave's
lag-time varies from zero to a value somewhat larger than 0.25 sec,
the signal should vary from complete interference with the direct wave
to maximum reinforcement. As a result, given elastic reflection at a
longitudinal wavespeed that averages 2620m/sec (from shot point to
ground-surface and back), full reinforcement should occur at a burial
depth somewhat greater than 330m. As it happens, our synthetic seismo-
grams for elastic reflection show maximum reinforcement at a depth of
about 450 m. However, factors other than the amplitude of seismometer

response enter the definition of m_b (see p. 35), which therefore reaches
its maximum value (assuming elastic reflection) at a depth of 870m.
For a granite medium with twice the longitudinal wavespeed of wet sand-
stone, maximum reinforcement of seismometer response (still assuming
elastic reflection) will occur at a burial depth very nearly twice 450m,
and m_b will probably attain its maximum at $\sim 2 \times 870m$ (or 1740m).

If we take into account cracking and the earth's gravitational field,
both the shape and amplitude of the reflected wave at teleseismic dis-
tances change with depth of burial. The head of the relief wave still
moves downward very nearly at seismic (elastic) speed; in fact, unload-
ing proceeds almost elastically until cracking occurs. For depths of
burial down to 1000m, however, the period of elastic unloading is
negligibly short. It ends when the medium cracks, a process that occurs
computationally as soon as the mean stress reaches zero (isotropic
cracking). Thus, cracking prevents the development of tension, effec-
tively limiting the amplitude of stress-relief waves to overburden
values. Subsequent recompression of the medium, due to its reassembly
under gravity, further reduces the amplitude of the relief wave--at
least as seen along rays that are almost vertically downgoing from the
shot point. Moreover, since the motion of cracked material is con-
trolled largely by gravity, development of the relief wave is slowed
by cracking: instead of progressing through continuous material at
elastic wavespeed, signals are repeatedly interrupted by cracks.

By increasing the time between direct- and relief-wave motions at
a given depth, gravity and cracking have the general effect of reducing
the shot-depth interval on which all reinforcement-interference phenomena
occur. Thus, body-wave magnitude varies more rapidly with depth in
Fig. 6 when gravity and cracking are taken into account than if they are
not. So do other features of seismometer response (see p. 35).

The combined effects of cracking and gravity are greatest for
shallow bursts. The farther the shot point from the ground surface
(increasing depth of burial), the weaker the initial wave when it
arrives at the surface and the more nearly elastic its reflection be-
comes. Thus, at "great enough" shot depths, the relief wave turns
into the pP-wave of elastic-half-space theory. Table 3, however, shows

Table 3

AMPLITUDE AND DURATION OF THE RELIEF WAVE DUE TO A 150-KT
BURST IN A WET-SANDSTONE HALF-SPACE VERSUS DEPTH OF BURIAL

The values tabulated refer to displacement along a downgoing ray from the shot point, 15° off the vertical. The term "Inelastic" refers to calculations that include cracking and gravitational forces, which are excluded from calculations termed "Elastic." The two types of calculation are otherwise identical. "Duration" = time between end of first period of downward displacement and attainment of peak upward displacement; amplitude = peak upward displacement.

Prob. #	Burial Depth(m)	Slant Range(m)	Relief-Wave Duration (sec)		Relief-Wave Amplitude (cm)	
			Elastic	Inelastic	Elastic	Inelastic
10/110	207.2	5290	0.10	0.33	1.87	0.58
12/112	531.3	4979	0.31	0.55	1.71	1.14
26/126	743.9	4775	0.43	0.70	1.96	1.29

quantitatively that reflection is far from elastic at shot depths of 200m to 750m. The table also shows that reflection becomes increasingly elastic as depth increases--but note that apart from the smallest of the three depths tabulated, higher multipoles of the field probably affect the durations and amplitudes listed. Large effects of gravity and cracking on reflected-wave motion are nevertheless demonstrated by Table 3, since the "Elastic" and "Inelastic" calculations differ in no other way than exclusion or inclusion of gravity and cracking. Those same effects are seen in still more detail in the displacement pulses of Fig. 7. In particular, note that at the shallowest burial depth, for which the displacements are due almost entirely to monopole radiation, hardly a jot remains of an otherwise-prominent pP-wave, when cracking and gravity are taken into account.

For all burial depths in Fig. 7, relatively early arrival of the first disturbance in the instance of gravity and cracking is due to an increase in p-wave speed with increasing overburden. By contrast, in all calculations without gravity and cracking, the sandstone half-space is considered homogeneous; its uniform p-wave speed is set to the value associated with overburden at a depth of 531m. Dispersion in a medium whose wavespeed increases with depth also accounts, in the main, for the lower peak displacement seen at each depth in Fig. 7 for calculations with gravity and cracking. Resistance to cavity growth that increases with shot depth is another consequence of variable overburden-- but a minor one--since the medium's shear-strength does not depend on mean stress. For a shot-depth of 207m, however, shear failure was observed in the relief wave as well as the direct wave. The field calculated for that shot depth assuming perfect reflection (see Fig. 7 for pulses) therefore differs from the other two fields (i.e., with gravity and cracking, and without). For all depths, moreover, perfect reflection eliminates mode conversion; all explosively generated energy then resides in an irrotational field, whence relief-wave amplitudes are larger for perfect reflection than if we merely suppress gravity and cracking.

Note that use of an isotropic model of cracking in the calculations tends to minimize crack formation, and hence to reduce associated
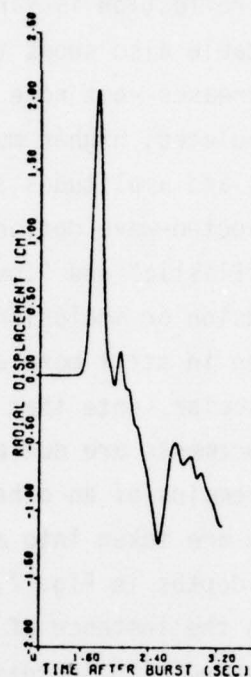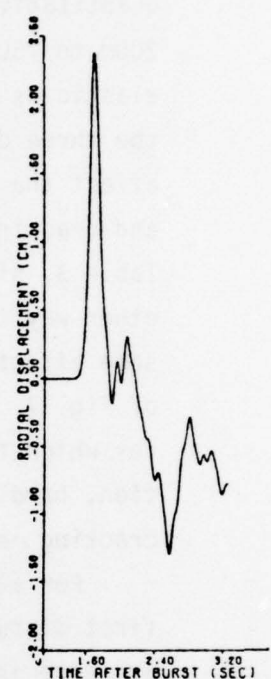
SHOT DEPTH=207m
RANGE=5290m
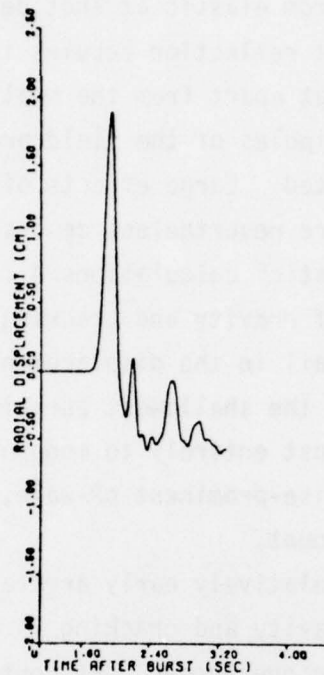
SHOT DEPTH=531m
RANGE=4979m

SHOT DEPTH=744m
RANGE-4775m

WITH
GRAVITY
AND
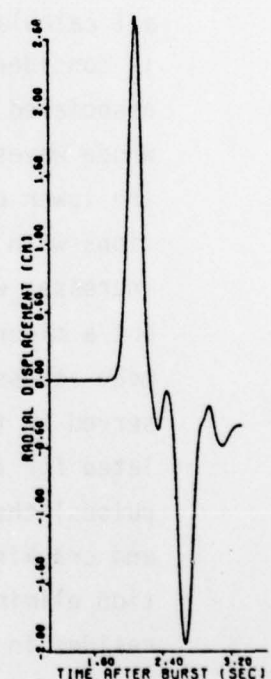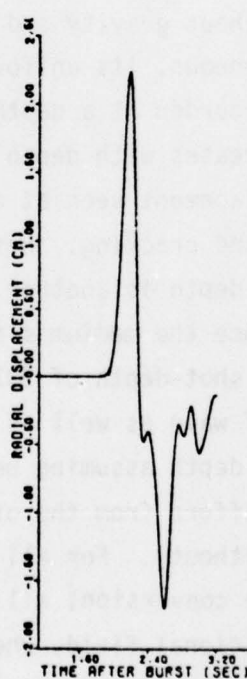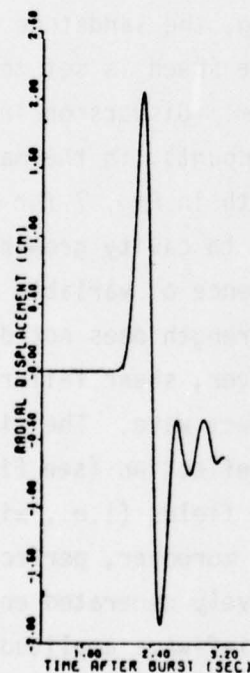CRACKING

WITHOUT
GRAVITY
AND
CRACKING

Fig. 7--Displacement pulses in the elastic near-field of a 150-kiloton
burst, for three depths of burial in a half-space of wet sand-
stone. The pulses refer to points of a down-going ray 15° off
the vertical, at distances from the shot point denoted by values
of "RANGE."

gravitational effects. We would therefore expect greater body-wave variations than those of Fig. 6, Table 3, and Fig. 7 to issue from calculations in which directional cracking is permitted. Also, the kind of minor seismogram wiggle that leads to a discontinuous change in m_b in Fig. 6 (p. 28) would almost certainly be ignored in practice. Instead, m_b-values would be obtained from a curve like 1'--for which our calculated variation of m_b with depth would be larger than 0.38 (the value quoted above, p. 27).

DISCONTINUITIES IN m_b

To better understand the results shown in Fig. 6 (p. 28), the specific definition of m_b (used in preparing the figure) must be consulted. In brief, of the several terms summed to give m_b, only one varies when depth of burial is changed. That term is $\log_{10}(A/TI)$, where, as calculated for Fig. 6, A is the difference between the most negative value of a seismometer's displacement; the following maximum value, T, is the time between the extremes of displacement represented in A; and I is an instrument correction that depends on T (and only T). Alternatively, A could be interpreted as the maximum swing of a seismometer over all pairs of consecutive extremes of its displacement. Fortunately, if m_b is defined in that way, no changes occur in curves 1, 1', and 2 of Fig. 6, and no important changes in curve 3. However, if A is taken as the difference between the most negative seismometer displacement and the most positive subsequent displacement, then curve 1 continues along 1' instead of dropping discontinuously.

A term like $\log_{10}(A/TI)$ appears in almost all definitions of body-wave magnitude (though often with I $\equiv$ 1), and leads directly to the sharp break seen (Fig. 6) in the m_b-depth curve for inelastic reflection at a depth of $\sim$575m, and in both curves for elastic reflection at $\sim$865m. Those breaks are true discontinuities. They occur because A, T, and (hence) I, are discontinuous functions of depth. In turn, jumps appear in A and T (hence, I) as functions of burial depth because the consecutive extremes of seismometer displacement that determine A and T can and do change abruptly with depth. In *their* turn, abrupt changes

occur in those extremes because the total response of the seismometer (a linear operator on ground displacement) is the sum of its individual responses to the direct wave, and to the relief wave, generated by any near-surface burst (p. 29). Depending on the delay between the two waves--and, hence, on burial depth--that sum may show all the extremes of each individual response; alternatively, a peak or trough of one response curve can overlie a peak or trough of the other, so that the two are fused into a single extreme of the complete seismogram. Thus, the number of extremes itself depends on burial depth. As a result, it is almost inevitable that sudden changes appear in the amplitude, A, of any given cycle of seismometer oscillation; for example, a "second maximum" whose value is used to compute A at one burial depth may be the third maximum at another depth. The approximate method by which curve 3 of Fig. 6 was constructed will now serve to show more concretely how discontinuities in m_b arise.

SPECIFICS OF INTERFERENCE AND REINFORCEMENT: APPROXIMATION OF PERFECT REFLECTION

Increasing the depth of a burst of given yield causes the relief wave originating at the ground surface to trail farther and farther behind the direct wave always created in such events (p. 29). In fact, as required by causality, the effects of reflection are delayed, relative to initial seismometer deflection, by a time equal to that of the first reverberation between shot point and ground-surface. Those effects are reviewed in detail here assuming reflection to be perfect. The relief wave then becomes the negative image, across the ground plane, of the direct wave; also, the ground plane becomes a surface dividing a uniform whole-space into two half-spaces.

Take first the instance of great lag (very deep burial), in which direct-wave displacements determine m_b. As a function of time at fixed position, those displacements form a pulse that looks like a positive half-cycle of a sine wave (positive displacement being away from the shot-point); a minor oscillation, due to spherical divergence of the field, also appears as the pulse ends. Accordingly, the seismometer at first moves away from the point of burst. Being an oscillator with

its own characteristic period (∿1 sec), it thereafter exhibits stages
of both positive and negative displacement as it swings about its equi-
librium position. Being a damped oscillator, it soon comes nearly to
rest. Thus, for a long while, the seismogram contains only two posi-
tive lobes, and one negative lobe, of consequence. Eventually, however,
the negative of that response appears, as the seismometer moves under
the influence of the relief wave reflected from the ground surface.
The individual seismometer responses, and their superposition to give
its total response, are shown in Fig. 8, along with both near- and far-
field pulses that define the displacement of ground material. For very
deep burial, the curve of total response--seismogram "A" of Fig. 8--is
duplicated when the individual responses are plotted. Simply put, the
two waves do not interact either as input to the seismometer or as
transformed by it.

A like set of plots is also shown in Fig. 8 for a shot depth of
890m. At that depth, individual responses to the direct wave and to
the relief wave do interact. The initial response of the seismometer
to the relief wave, which is negative, occurs at such time as to inter-
fere with its second positive outward swing in response to the direct
wave. A minor oscillation is thereby introduced into the latter re-
sponse curve. At a slightly shallower burial depth (860m), and hence
smaller lag-time, overlap of the initial negative relief-wave response
with the second positive direct-wave response is reduced. As a result,
the low-amplitude maximum-minimum oscillation of seismogram B is de-
graded to a dimple in a curve of constantly increasing displacement
(seismogram C of Fig. 8).

The change from seismogram B to seismogram C has evidently taken
place continuously with depth. It is equally clear, however, that the
difference between the all-time minimum displacement and next maximum
(A_1, say) has changed discontinuously, and with it the time between
those two extremes. So has the maximum displacement-swing found among
all pairs of consecutive extremes (A_2, say); that swing occurs between
points 5 and 6 of seismogram B (point 5, the earlier of the two, is a
maximum), and points 2 and 3 of seismogram C (the earlier point, 2, is
a minimum). Thus, if A_1 or A_2 is taken as the amplitude A, and T is

38

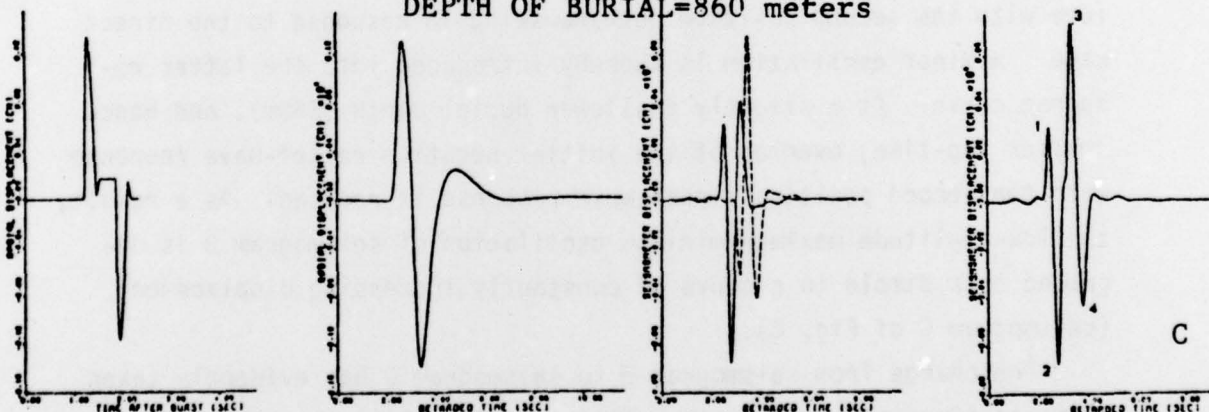## VERY DEEP BURIAL

A
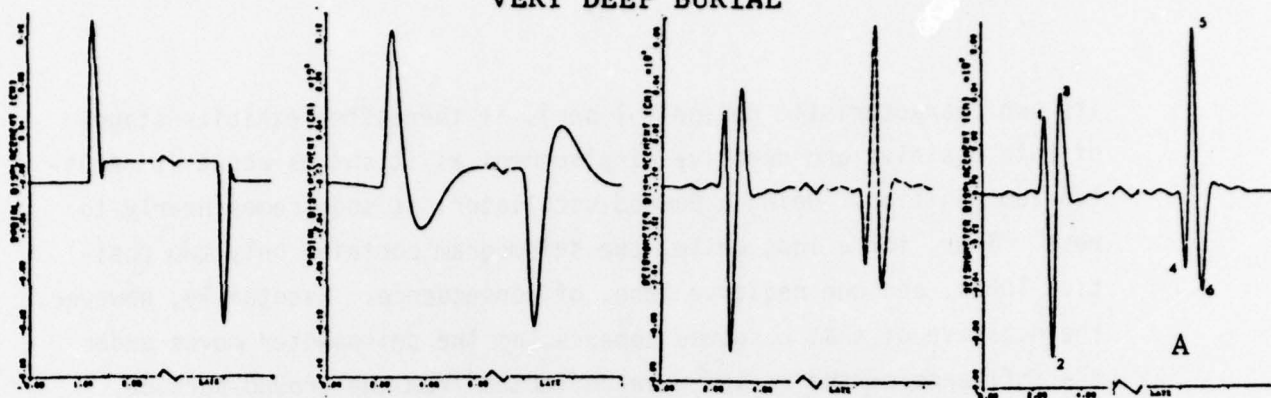
DEPTH OF BURIAL=890 meters

B
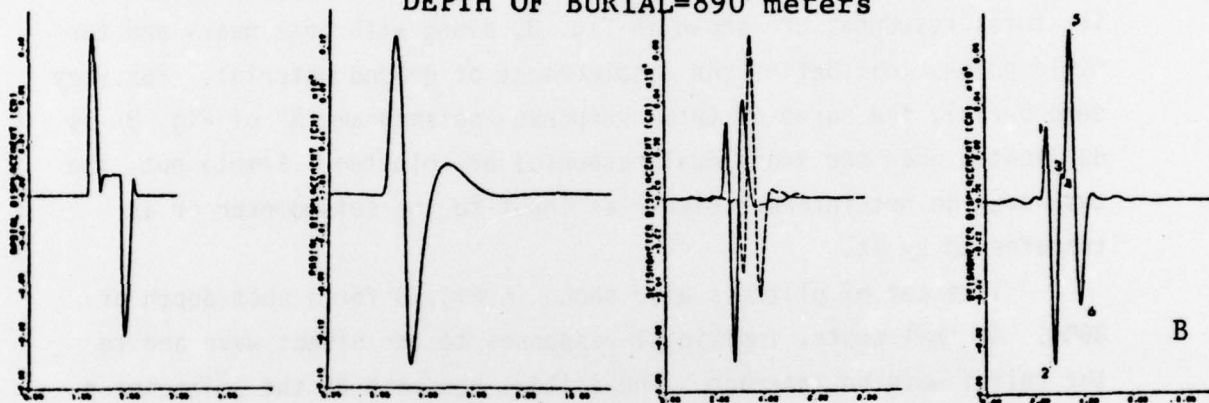
DEPTH OF BURIAL=860 meters

C

| NEAR FIELD | FAR FIELD | TWO RESPONSES | TOTAL RESPONSE |

Fig. 8--Ground motion and seismometer response: 150-kiloton burst in a
wet-sandstone half-space; perfect ground-surface reflection; three
burial depths. From left to right, the four curves for each shot
depth show, vs. time, 1) displacement of material along a down-
going ray 15° off the vertical, 100 kilometers (km) from the shot,
2) displacement on that ray at 5000 km ("FAR FIELD"), 3) separate
far-field seismometer responses to the direct wave and relief wave
("TWO RESPONSES"), and 4) total seismometer response.

equated to the time between the extremes that determine A, then the term $\log_{10}(A/TI)$ will jump on varying the shot depth from 890m (case B) to 860m (case C). In deriving curves 1, 2, and 3 of Fig. 6 (p. 28), a definition of A_1-type was chosen for A (i.e., from all-time minimum displacement to the next maximum), which led to the discontinuities seen in the figure. On the other hand, switching to a definition of A_2-type would leave curves 1 and 2 unchanged, as well as the depth at which curve 3 jumps. As just noted, however, the size of the jump would change in the instance of perfect reflection (curve 3 of Fig. 6); points 2 and 3 of seismogram B determine m_b if A is A_1-like, and points 5 and 6 if A is A_2-like.

A transition from the pattern of seismometer deflection seen in seismogram C to that of seismogram B is evident in Fig. 9. Figure 9 contains plots like those of Fig. 8 ("Two Responses" excepted), but applies to our full-blown calculations of motion with gravity and cracking. For the corresponding calculations without gravity and cracking, only pattern C appears (Fig. 10); at burial depths less than $\sim$870m, some mechanism must act to enhance lag-time, as gravity and cracking do (p. 33), or else direct- and relief-wave responses will not be separated enough to produce pattern B.

As burial depth is reduced from 860m in the instance of perfect reflection, the initial negative relief-wave response (R_1^-, say) overlaps more and more fully the first negative direct-wave response (D_1^-). Since D_1^- has more than twice the amplitude of R_1^-, however, only a modest increase (30 to 40 percent) takes place in the swing between the first minimum of seismometer deflection (point 2 of seismograms A, B, C), and either the next-earlier or next-later maximum (point 1 or point 3). Most of the latter amplitude increase with decreasing depth (i.e., between points 2 and 3) is due to reinforcement of the second positive direct-wave response by the first positive relief-wave response.

Major changes occur in the value of A that enters m_b only when burial depths become so shallow (<400m) that the first positive relief-wave response starts to cancel its image (the first negative direct-wave response). As shot depth is further decreased, the amplitude A drops at an ever-increasing rate and, with it, m_b itself. The same
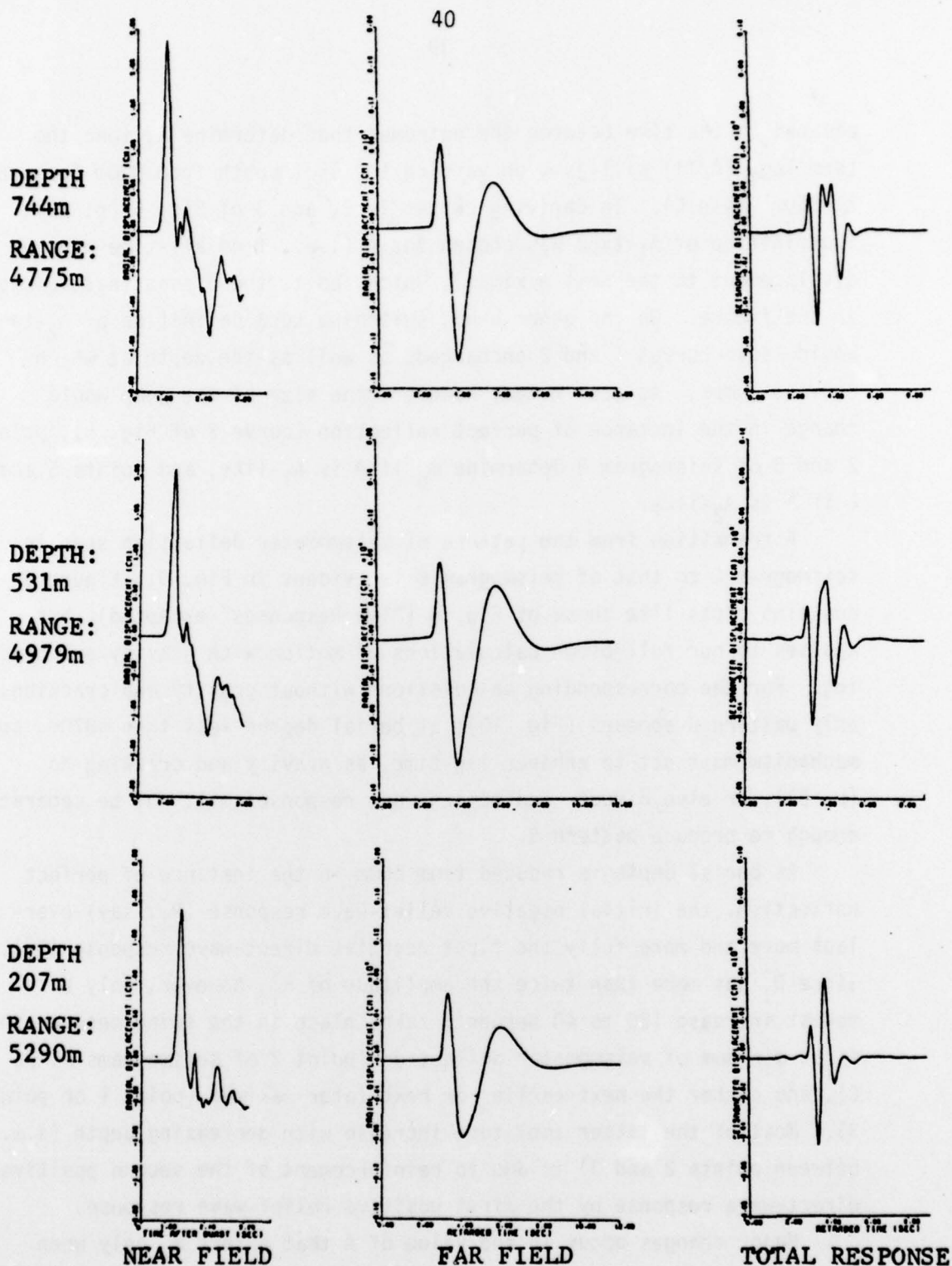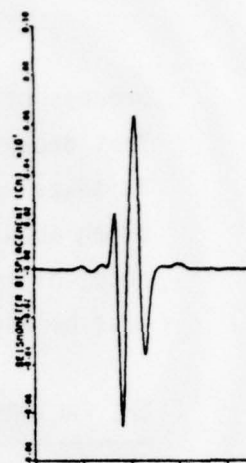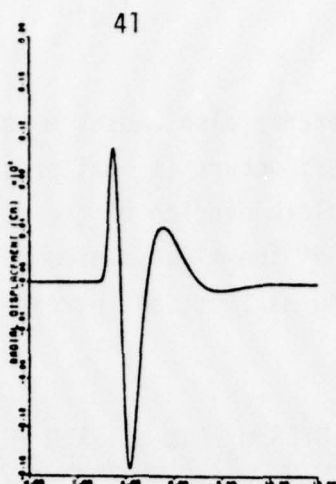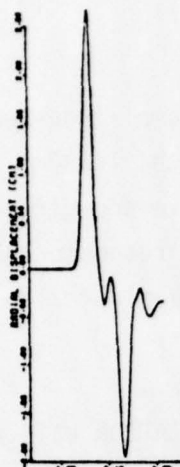
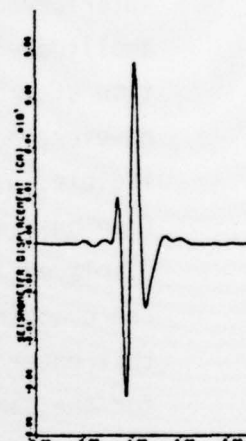NEAR FIELD   FAR FIELD   TOTAL RESPONSE

Fig. 9--Near- and far-field displacement pulses, and seismometer responses, for
150-kiloton bursts at three depths in a wet-sandstone half-space, calcu-
lated *with* gravity and cracking. The pulses refer to points of a down-
going ray 15° off the vertical, at near-field distances from shot point
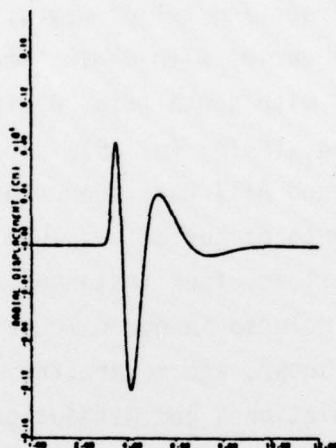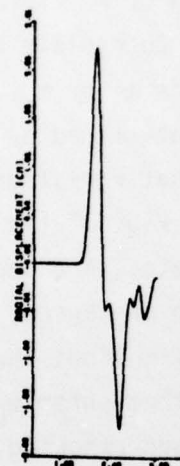denoted by "RANGE"; the far field is 5000-km away.

Fig. 10--Near- and far-field displacement pulses, and seismometer responses, for 150-kiloton bursts at three depths in a wet-sandstone half-space, calculated *without* gravity and cracking. The pulses refer to points of a down-going ray 15° off the vertical, at near-field distances from shot point denoted by "RANGE"; the far field is 5000-km away.
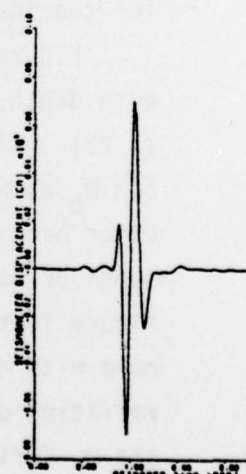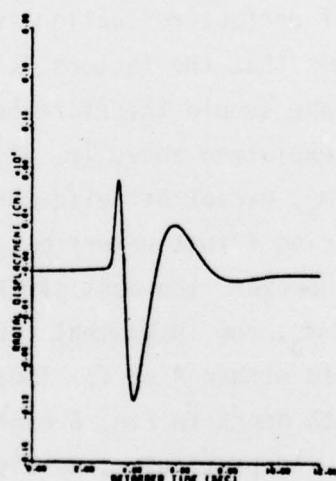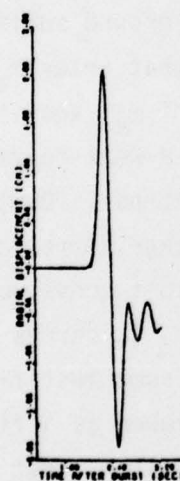
process of interference also causes m_a and its amplitude-factor to fall.
That decay, however, occurs at smaller shot depths (<200m) than for m_b:
it takes more complete overlap of the relief wave and direct wave to
bring about decay of the first minimum of total response than to effect
decay of the second maximum; to increase the waves' overlap, shot depth
must be reduced.

THE FACTORS THAT ENTER m_a AND m_b, AND THEIR VARIATION WITH DEPTH

Figure 8, and the discussion just concluded of reinforcement and
interference of direct and relief waves, serves to explain how the
amplitude-factor A varies with depth, whether for m_a or m_b. The varia-
tion of m_b (or m_a) with depth (Fig. 6) is not determined by A alone,
however, but by $\log_{10}(A/TI)$ (p. 35). To make that variation intel-
ligible, A, T, I, and A/TI have been plotted in Fig. 11 (in semilog
fashion) versus depth of burial. Values of A, etc., are separately
displayed in Fig. 11 for four instances. In two instances, gravity
and cracking are included in our calculations of motion; the values
that enter m_a are shown, and so are the values that enter m_b. Then,
for the same calculations, but without gravity and cracking, the fac-
tors A, etc., are plotted; in addition, the figure contains m_b-factors
for the instance of perfect reflection from the ground surface.

Figure 11 shows that the factors A, etc., that enter m_a vary little
with depth. The same should therefore be true of m_a, and it is (Fig. 6,
p. 28). Also, as explained above (p. 35), A is a weak function of depth
for m_b as well as m_a, except at quite shallow depths (<200m). On the
other hand, the period T that enters m_b does change appreciably with
depth of burial. However, the most striking result conveyed by the
figure is that for m_b, the instrument correction, I, varies a good deal
more with depth than either A or T. Thus, with some justification, the
variation of m_b with depth in Fig. 6 might be viewed as a figment of
the m_b-definition. In particular, as discussed below, most of the
depth-dependence of m_b would disappear if the term $\log_{10}A/TI$ were re-
placed by $\log_{10}A$ in defining m_b. Yet, that view is not exhaustive:
the dependence of T on shot depth, from which the variation of I follows,
is real (though as already noted, and as Fig. 11 shows, gravity and
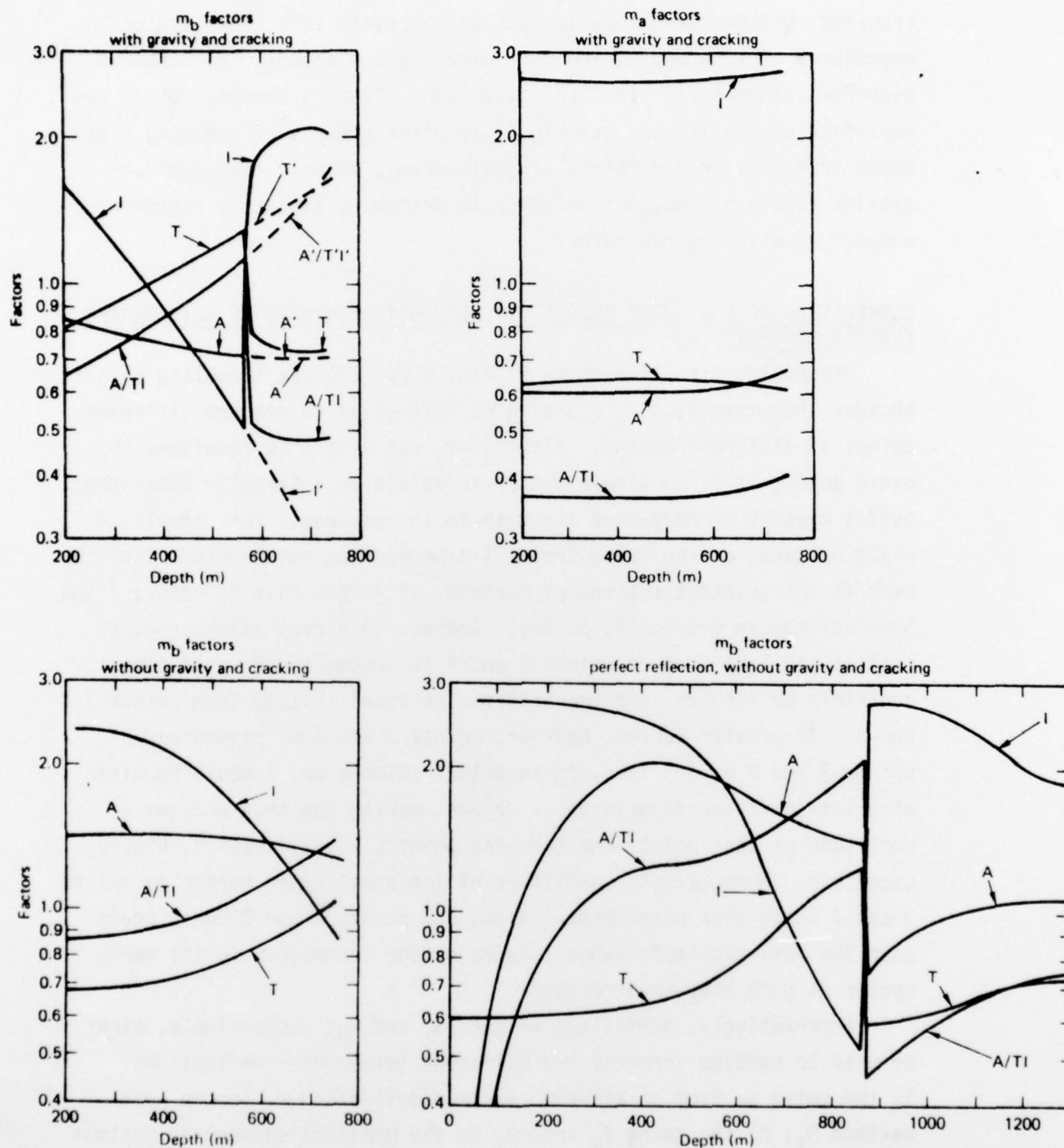
Fig. 11--Three depth-dependent factors that determine body-wave magnitudes m_a and m_b, versus shot depth, for 150-kiloton bursts in a wet-sandstone half-space. Amplitude A is equal to the seismometer deflection from its all-time minimum, either to its next-earlier maximum (m_a), or to its next-later maximum (m_b). T is twice the time-interval between the extremes that define A; the instrument correction I varies with T only. Changes in magnitude with depth are identical to changes in $\log_{10}(A/TI)$--also shown.

cracking must be taken into account to calculate it). The strong dependence of I on depth, and more directly the changes in T that it signifies, therefore have a positive side. Those T-changes, which are amplified by gravity and cracking, may offer a means of deducing shot depth from the early portions of seismograms, whereas the same data provide values of $\log_{10}A$ from which to determine explosive yield--a subject to which we now turn.

CORRELATION OF BODY-WAVE SOURCE STRENGTH WITH FEATURES OF SEISMOGRAMS: FURTHER COMMENTS

Discontinuities like those of Fig. 6 (p. 28) are troubling chiefly because they mean that m_b has been so defined as to measure different things at different depths. Although m_b can easily be redefined to avoid jumps, it is no simple matter to obtain an internally consistent, useful measure of body-wave strength in the process. For example, A could be taken as the swing from all-time minimum seismometer displacement to the greatest subsequent maximum, as in the case of points 2 and 5 of seismogram B (Fig. 8, p. 38). Indeed, in a real seismogram, an oscillation like that of points 3 and 4 in seismogram B would almost certainly be ignored, and the A-factor reckoned instead from points 2 and 5. At greater depths, however, points 2 and 5 of seismogram B become 2 and 5 of A. Thus, in an actual seismogram, 5 would be mixed with late-arriving signals of all kinds, making the true body-wave amplitude at that point, and even the point's identification, highly uncertain. Moreover, the amplitude of the oscillation marked by points 3 and 4 would then have become large, and points 2 and 3 would again span the full amplitude-range covered by the seismogram in its early cycles of pure body-wave response.

Alternatively, normalized weights w_1 and w_2, respectively, might be used to combine linearly two different seismometer deflections: 1) the swing S_1 from an all-time minimum deflection m_1 to the next maximum M_1; 2) the swing S_2 from m_1 to the greatest subsequent maximum. Weight w_2 could be made a smooth function of the time T_2 taken to complete swing S_2, with the value of the function equal to zero when T_2 exceeds a specified multiple of the period covered by S_1; w_1 would vanish smoothly as zero is approached by the time from maximum M_1 to

the next minimum (e.g., from point 3 to point 4 of the seismogram B in Fig. 8). As we see it, little of value is likely to emerge from such algebraic thrashing about, because it does nothing to solve the basic problem of untangling the direct wave and relief from one another. For example, if a weighted average like that described above were used to compute the factor A, then m_b would still measure two different things at different depths--albeit with a smooth transition from one thing to the other.

On balance, given its near-freedom from relief-wave influence for all but cratering bursts, m_a seems more closely related than m_b to body-wave strength--yet it too has drawbacks. For one, the amplitude of the first significant positive swing of the seismometer is low relative to those of its subsequent swings, and is often lost in background noise. In most instances, the factor A is therefore appreciably smaller for m_a than m_b, though not by more than a factor of two. As a result, the minimum yield for detection of explosions is somewhat higher when m_a is used rather than m_b. More serious are the large effects of back-ground noise on the period T that enters m_a, as opposed to m_b--effects magnified by the instrument correction, I. For example, noise that makes the first maximum uncertain by a factor of two may only alter A by 10 percent to 20 percent while giving rise to a 40-percent error in T and a still larger error in the product TI. Moreover, the first maximum of seismometer response is likely to be more sensitive to variations in site medium than are its later extremes of deflection.

The difficulties cited lead us to suggest that the A-factor alone be used in place of A/TI as a measure of body-wave strength. Indeed, according to Figs. 6 and 11 (pp. 28 and 43), relief-wave effects on m_b, including its discontinuity, are much larger than on the value of log A that enters m_b. We therefore consider $\log_{10} A$ a better index of body-wave strength than the m_b quantity to which it contributes. A combination of that value of $\log_{10} A$ with m_a (or the A-factor associated therewith) might be more useful still.

47

REFERENCES

1. Trulio, J., "Ejecta Formation: Calculated Motion from a Shallow-Buried Nuclear Burst, and Its Significance for High Velocity Impact Cratering," *Impact and Explosion Cratering* (Proceedings of the Symposium on Planetary Cratering Mechanics; Flagstaff, Arizona, 13-17 September 1976), pp. 919-957.

2. Cherry, J., T. Barker, S. Day, and P. Coleman, "Seismic Ground Motion from Free-Field and Underburied Explosive Sources," Sec. IV, Final Report No. SSS-R-77-3349 under ARPA Order No. 2551, July 1977.

3. Lee, L., and J. Malthan, *The Cagniard Method for Investigating Edge Effects in the High-Explosive Simulation Technique (HEST) Project HEST Test V*, Technical Report No. AFSWC-TR-68-27, February 1969.

4. Trulio, J., N. Perl, and G. Balanis, *The AFTON 2A Computer Code Revised User's Manual*, Part 1, Theory and Explanations, AFWL-TR-75-111, June 1976.

5. Harkrider, D. G., "Surface Waves in Multilayered Elastic Media. I. Rayleigh and Love Waves from Buried Sources in a Multi-layered Elastic Half-Space," *Bull. Seism. Soc. Am.*, Vol. 54, 1964, p. 627.

6. Bache, T. C., J. F. Masso, and B. V. Mason, *Theoretical Body and Surface Wave Magnitudes for Twelve Numerically Simulated Cratering Explosions*, Systems, Science and Software Report SSS-R-77-3119, La Jolla, California, January 1977.

7. Marshall, P. D., and P. W. Basham, "Discrimination Between Earthquakes and Underground Explosions Employing an Improved M_S Scale," *Geophys. J.R. Astro. Soc.*, Vol. 28, 1972, p. 431.

8. McEvilly, T. V., "Central U.S. Crust--Upper Mantle Structure from Love and Rayleigh Wave Phase Velocity Inversions," *Bull. Seism. Soc. Am.*, Vol. 54, 1964, p. 1997.

9. Knopoff, L., "Q," *Rev. Geophys.*, Vol. 2, 1964, p. 625.

10. Tryggvason, E., "Dissipation of Rayleigh Wave Energy," *Journ. Geophys. Res.*, Vol. 70, 1965, p. 1449.

11. Pacific-Sierra Research Corporation, Internal Memorandum, 1977.

12. Richter, C. F., *Elementary Seismology*, W. H. Freeman and Co., Inc., San Francisco, 1958.

13. Perl, N., Applied Theory, Inc., Private Communication, 1978.

14. Bache, T., et al., *Teleseismic Verification of Data Exchange Yields*, Topical Report No. SSS-R-76-2941 under ARPA Order No. 2551, May 1976, pp. 28-31.

REPORT DOCUMENTATION PAGE		READ INSTRUCTIONS BEFORE COMPLETING FORM
1. REPORT NUMBER	2. GOVT ACCESSION NO.	3. RECIPIENT'S CATALOG NUMBER
4. TITLE (and Subtitle) EFFECT OF BURIAL DEPTH ON SEISMIC SIGNALS. Volume I.		5. TYPE OF REPORT & PERIOD COVERED Final report, 1976-78
		6. PERFORMING ORG. REPORT NUMBER PSR-815-VOL-1
7. AUTHOR(s) N. Perl; W. L. Woodie F. Thomas J. Trulio Frank J.		8. CONTRACT OR GRANT NUMBER(s) DNA001-76-C-0078; ARPA Order 3099
9. PERFORMING ORGANIZATION NAME AND ADDRESS Pacific-Sierra Research Corp. 1456 Cloverfield Blvd. Santa Monica, Ca. 90404		10. PROGRAM ELEMENT, PROJECT, TASK AREA & WORK UNIT NUMBERS Project No. ARPA Order 3099 ARPA Code No. 6F10. Program Element Code No. 62701E
11. CONTROLLING OFFICE NAME AND ADDRESS Defense Advanced Research Projects Agency 1500 Wilson Blvd. Arlington, Virginia 22209		12. REPORT DATE May 1979
		13. NUMBER OF PAGES 47(Vol. I), 198(Vol. II)
14. MONITORING AGENCY NAME & ADDRESS(if different from Controlling Office) Defense Nuclear Agency Washington, D.C. 20305		15. SECURITY CLASS. (of this report) Unclassified
		15a. DECLASSIFICATION/DOWNGRADING SCHEDULE

16. DISTRIBUTION STATEMENT (of this Report)

Approved for public release, distribution unlimited

17. DISTRIBUTION STATEMENT (of the abstract entered in Block 20, if different from Report)

18. SUPPLEMENTARY NOTES

19. KEY WORDS (Continue on reverse side if necessary and identify by block number)

Nuclear explosion seismology
Surface wave magnitude
Body wave magnitude

Nuclear explosion seismic coupling
Yield estimates

20. ABSTRACT (Continue on reverse side if necessary and identify by block number)

This report discusses a calculational program aimed at improving the U.S. capability to verify a Threshold Test Ban Treaty (TTBT) by seismic means. The analysis emphasizes shallow bursts, examining both body-wave and surface-wave effects. Two-dimensional inelastic source calculations, using Applied Theory's AFTON program, were made on a representative set of 150 KT explosions.

Simple elastic theory is reviewed, indicating that the primary body wave from a buried explosion receives positive or negative reinforcement from the free-surface reflection. The more refined calculations, which include inelastic and

DD FORM 1473 EDITION OF 1 NOV 55 IS OBSOLETE
1 JAN 73

gravitational effects, indicate a "reflection" amplitude smaller than that cal-
culated for the elastic case. More important, the reflected wave is relatively
delayed in time, so that transitions between positive and negative reinforce-
ment occur at shallower depths of burial.

A surface-wave model is developed, based on Green's function. Many prob-
lems were encountered in modifying the AFTON source-data program to provide
information that was accurate for long-period displacements, and to extrapolate
calculations well beyond the reasonable truncation times for the program.

Preliminary conclusions are made concerning the need for inelastic source
calculations; depth-of-burial effects on signal generation; the resulting yield
estimation; possible improved yield estimation procedures; and topographic
effects.

Volume I presents summaries of the body-wave and surface-wave calculations
to date. Volume II includes additional details and numerical methods.